Title

Mesoscale Characterization of Observed and Simulated Surface Winds During Post-tropical Cyclone Sandy's Landfall

Authors

James A. Schiavone[1], David A. Robinson[2], Peter Johnsen[3], Mathieu Gerbush[2] and Alan Norton[4]

[1] Independent scientist, Bridgewater, New Jersey, corresponding author, jimschiavone@gmail.com

[2] Rutgers University, Piscataway, New Jersey

[3] Cray Inc., Bloomington, Minnesota

[4] National Center for Atmospheric Research, Boulder, Colorado

Abstract

Post-tropical cyclone Sandy was significant because of intense flooding and wind damage it inflicted on a large footprint of a dense metropolis and its rare track and extratropical transition just before landfall. Fortuitously, it also represented a post-event research opportunity because of mesonet systems that survived landfall and a 500 meter resolution Weather Research and Forecasting (WRF) simulation executed only months later. Temporal, geographical and probability distributions of wind speed are reported for the landfall region and period. The simulation is used to interpret mechanisms driving surface winds and quantitative comparisons are reported between observed and simulated wind speeds. Highest observed winds over land occurred at New Jersey coastal extremities, with a primary maximum south of Sandy Hook and a secondary near Cape May. Signatures of large eddy circulations (LEC) appear in radar and surface observations and in WRF over northern New Jersey and Pennsylvania throughout landfall. They exhibit 8 km wavelengths, propagate toward west-northwest, and are similar to those reported elsewhere. WRF land use categorization greatly influences spatial variability of predicted surface speeds and WRF over-predicts speeds at all land locations and times except for northern coastal New Jersey during and after landfall, consistent with a known WRF land-based wind speed bias. To improve accuracy and resolution of surface wind speed predictions during land-falling tropical cyclones, it is recommended to use finer resolution and categorization of land surface roughness fields, include topographic roughness in roughness representations, and use boundary layer parameterizations that explicitly represent vertical momentum transport by LECs.

1. Introduction

Post-tropical cyclone Sandy made landfall on New Jersey at about 2330 UTC 29 October 2012 and was exceptional in many ways – its rare track, its size, its extratropical transition (ET) just prior to landfall and associated late secondary intensification, and the extensive damage it caused to a major coastal metropolitan area from both storm surge and wind. Fortuitously, understanding the fine structure of this storm during its landfall on New Jersey is aided considerably by two key resources: (1) the pair of resilient mesonets, the New Jersey Weather Network (NJWxNet) and the Delaware Environmental Observing System (DEOS), that continued to log surface observations throughout the storm and (2) a 500 meter resolution, 4 billion grid point, Weather Research and Forecasting (WRF) simulation that was run on the Cray XE6 "Blue Waters" at the National Center for Supercomputing Applications (NCSA).

a. Relevant prior work

Because post-tropical cyclone Sandy was exceptional, already it has been the subject of many investigations, especially forecast accuracy studies of track, intensity and inundation. Track and intensity predictions from most models were highly accurate while the storm was over the open ocean, but details diverged as the storm neared the coastline. Sensitivity of forecasts to initial and boundary conditions, as well as to different numerical weather prediction models, has been a significant topic of study (Bassill 2014, Galarneau et al. 2013, Kowaleski and Evans 2016, Lussier III et al. 2015, Magnusson et al. 2013, Magnusson et al. 2014, McNally et al. 2014, Munsell and Zhang 2014, Torn et al. 2015, Zhu et al. 2017). Prior work also covers storm surge forecasts (e.g., Alves et al. 2015, Blumberg et al. 2015, Drews and Galarneau 2015, Forbes et al. 2014, Wang et al. 2014), the potential role of climate change (e.g., Greene et al. 2013, Lackmann 2015, Sobel 2014, Xiang et al. 2015) and other topics (e.g., Bosart 2013, Good et al. 2014, Keighton et al. 2016, Vigh et al. 2013).

Pertinent to surface winds associated with land-falling hurricanes, which is a key focus of this work, are recent studies of the planetary boundary layer (PBL) parameterization schemes (Balzarini 2014, Bretherton and Park 2009, Cohen et al. 2015, Grenier and Bretherton 2001, Janjic 1994, Nakanishi and Niino 2006, Shin and Hong 2011, Sukoriansky et al. 2006, Xie and Fung 2014), particularly those that focus on surface wind fields and the influence of mesoscale tropical cyclone features that impact those winds (Braun and Tao 2000, Davis et al. 2008, Gopalakrishnan et al. 2013, Hill and Lackmann 2009, Nolan et al. 2009, Yang et al. 2008, Zhang 2016, Zhang and Uhlhorn 2012, Zhang and Pu 2017). Roll vortices, also known as large eddy circulations (LEC), are documented theoretically (Foster 2005) and exhibited in radar observations (Gall et al. 1998, Katsaros et al. 2000, Katsaros et al. 2002, Lorsolo et al. 2008, Morrison et al. 2005, Wurman and Winslow 1998) and simulations (Bryan et al. 2017, Gao and Ginis 2016, Green and Zhang 2015a, Green and Zhang 2015b, Nakanishi and Niino 2012, Zhang et al. 2008, Zhu 2008) of tropical cyclones. They are found to have wavelengths in the range of

0.2 to 10 km and are an important topic of active research. Their study is facilitated by increases in model resolution and they are found to play an important role in vertical transport of energy in the hurricane boundary layer (HBL), and thus, an important role in forecasting intensity of tropical cyclones. LECs are also potential drivers of localized high winds in tropical cyclones that can cause localized destruction of property and tree-fall-induced utility infrastructure damage (Ramstrom et al. 2016). Finally, LECs potentially affect the fine structure of wind fields in tropical cyclones and better representing LECs in models can potentially improve storm surge forecasting in coastal estuaries.

Pertinent to using higher resolution simulations of wind fields in the PBL, such as the 500 meter horizontal resolution WRF simulation of this study, there exists a body of recent research that addresses the "turbulent grey zone" of model resolution that spans the 100 through 1,000 meter range. Research in this realm is very important for quantifying vertical transport in the PBL that drives extreme surface winds and dynamics of overall hurricane intensity (Green and Zhang 2015b, Zhang and Pu 2017, Zhang et al. 2017), since this is the zone where large, anisotropic, energy-containing turbulent eddies become partially resolved (Wyngaard 2004). It is estimated that the 500 meter resolution WRF simulation studied herein likely has a 50%/50% split of resolved and sub-grid total kinetic energy (Shin and Hong 2015). More specifically, in the HBL, classic K-theory PBL parameterization schemes are unable to realistically represent turbulent processes and vertical transport (Gao and Ginis 2016, Green and Zhang 2015b, Shin and Dudhia 2015, Zhu 2008). These schemes do not represent vertical transport by LECs (Gao and Ginis 2016, Zhu 2008) and discourage development of strong, localized, transient wind gusts near the ground (Green and Zhang 2015b).

Comparisons of different WRF PBL parameterization schemes for application to the HBL show that the Mellor-Yamada-Janjic (MYJ) scheme performs better than the Yonsei University (YSU) scheme for the HBL over land because it can handle upstream roughness (Nolan 2012) and that the Mellor-Yamada (MY) scheme performs better than YSU for the HBL in general mainly because of YSU's strong dependence on a diagnosed PBL height (Kepert 2012). However, because the PBL parameterization assumptions begin to fail below 1 km resolution, PBL schemes must be replaced by others akin to large eddy simulations (LES) in this resolution range (Ito et al. 2016, Mirocha et al. 2010, Worsnop 2016). New HBL schemes are recommended and proposed by Zhu (2008) and Gao and Ginis (2016). Even beyond tropical cyclones, WRF was discovered to be biased for surface wind speeds over land, with WRF speeds too high (low) over plains and valleys (hills and ridges) (Cheng and Steenburgh 2005, Frediani et al. 2016, Mass and Ovens 2010, Roux et al. 2009, Santos-Alamillas et al. 2013). This topography bias is corrected by a new WRF surface layer scheme (Jimenez and Dudhia 2012).

b. Background on this work

The aim of this work is to leverage the resilient mesonets and the 500 meter resolution WRF simulation to characterize the mesoscale fine structure of surface wind fields observed during Sandy's landfall, to understand the mechanisms driving wind fields and to characterize the late-stage extratropical transition and associated air streams and their evolution (Schiavone et al. 2016). Since the WRF simulation output is a key resource, a final aim is to evaluate performance of the 500 meter resolution WRF simulation during landfall.

The scope of this work is (1) over land, where in-situ observations are most dense; (2) at the surface, where population impact exists; (3) focused on wind speed, for interests of multiple hazards such as wind damage to property and utility infrastructure and wind forcing for inundation predictions; (4) during landfall, to capture detail during this critical time window; (5) observational, to characterize the fine-scale spatial and temporal distribution of winds; and (6) interpretational, by using the 500 meter resolution WRF output to interpret the observations. Publication size limitations constrain this report to an initial characterization and foray into understanding surface winds during Sandy's landfall from a broad perspective. Subsequent papers will delve more deeply into specific topics.

c. Paper organization

This paper is organized as follows. Section 2 describes data sources and specific meteorological variables studied. Section 3 provides an overview of Hurricane Sandy and describes landfall in more detail. Section 4 presents analyses of observed and simulated winds. Section 5 discusses the impact of PBL and physiographic features on winds and recommends ways to improve predictions of surface wind fields for land-falling tropical cyclones. Section 6 summarizes key results. Animations are available on SeedMe.org at links denoted by Fig. S-N, where N is the supplementary figure number. Supplemental Material describes data dissection and visualization methods, adjustment of wind speed for anemometer height, validation of WRF simulated variables by comparison with profile observations, PBL stability, comparison with inundation forecasts and plans for future work. It also contains links to animations and their captions.

2. Data

a. Sources

Observations used in this work comprise surface and profile observations and radar data, as summarized in Table 1 with sites located on a map in Fig. 1. Surface observations are from a pair of state mesonets, NJWxNet and DEOS, supplemented with neighboring data from NOAA Automated Surface Observing System (ASOS) and National Data Buoy Center (NDBC) stations, comprising a set of 126 surface stations. Profile observations are from the 3 nearest

5

rawinsonde stations, Upton, NY (OKX), Wallops Island, VA (WAL) and Sterling, VA (IAD), as well as from vertical azimuthal displays (VAD) of wind profiles from the Fort Dix, NJ (DIX) WSR-88D radar site. Reflectivity and radial velocity data were also used from the latter.

Simulation data is from a 96 hour simulation using Advanced Research WRF version 3.3.1 initialized at 1200 UTC 26 October 2012 (Johnsen et al. 2013), for which details are presented in Table 2. NOAA/NCEP GFS global model output was used for initialization and boundary conditions and 224 Gigabytes of output were archived every half-hour for a total of 43 Terabytes. The grid size was 5320x5000 with 150 layers and execution required 58 hours using 140,000 cores (CPUs). The simulation was run on the Cray XE6 "Blue Waters" at NCSA just after it came online in March 2013. Note that both simulation and mesonet data were leveraged for this study *after* they were archived and, thus, it was not possible to tailor them to specific needs of this work.

b. *Variables studied and their characteristics*

Although surface wind speed and direction observations were the focus of this study, surface temperature observations were also used. Surface observation intervals are 5 minutes except for NDBC, which varies from 5 to 60 minutes by site. Wind speed sampling and averaging differs among surface observation networks. Although networks record more than one metric for wind speed, a single metric was chosen to facilitate comparison. For wind speed and direction, NJWxNet records a single instantaneous sample every 5 minutes, DEOS records an average of 15 equally-spaced instantaneous samples every 5 minutes and ASOS records 2-minute averages every 5 minutes.

Comparable surface variables from the WRF simulation were used: wind speed and direction at 10 meter elevation and temperature at 2 meter elevation. Surface water vapor mixing ratio was also used, although the latter variable was not comprehensibly available for mesonet stations. By comparison with observed measurements of wind, WRF 10 meter wind speeds represent averages over about 1 to 6 minutes, depending on actual wind speed. As found by Skamarock (2004) using kinetic energy spectra analyses, WRF's effective horizontal resolution is about 7 times the grid spacing. Thus, WRF's effective averaging time for 35 m s^{-1} wind speeds, for example, is about 7x500/35 = 100 seconds. Mesonet and NDBC anemometer heights that are not 10 meters are adjusted to 10 meters by fitting a logarithmic wind profile to wind speed averages for stations having anemometers at the two most common heights, 10 and 3 meters, as described in the Supplement's section S-2.

Analogous profile variables were also used for the rawinsonde observations: wind speed and direction, temperature and water vapor mixing ratio.

3. Landfall characterization

This section presents a *qualitative* characterization of Sandy's structure and evolution during the landfall period, based on both surface observations and interpretation of the simulation. Section 4 presents a *quantitative* analysis of observations and their comparison with the simulation.

a. Sandy overview

A westward-propagating tropical wave that entered the Caribbean Sea by 19 October 2012 intensified sufficiently to have been named Tropical Storm Sandy (Blake et al. 2013) by the National Hurricane Center (NHC) on 23 October. The storm looped northward (Fig. 2) and continued to intensify to hurricane strength by 25 October, reaching category 3 (Simpson 1974) intensity just prior to traversing Cuba's eastern end late that day. Sandy weakened quickly after crossing Cuba, mainly because of strong southwesterly wind shear, but continued to track northward through the Bahamas as a category 1 storm through 26 October. Hurricane Sandy continued to expand in size, however, even as it weakened to a temporary intensity minimum on 27 October as it exited the Bahamas and turned to the northeast, travelling parallel to the Carolina coast. Re-intensification began on 28 October as Sandy traversed warm Gulf Stream waters (Galarneau et al. 2013) and continued intensifying more rapidly on 29 October just before being turned toward the northwest by a strong, eastward-propagating, mid-tropospheric wave. Landfall occurred near Brigantine, NJ around 2330 UTC 29 October 2012 with 36 m s^{-1} sustained winds (Blake et al. 2013). Since landfall time cannot be precisely specified, a nominal landfall time of 0000 UTC 30 October 2012 is used herein.

Figure 3 shows the NHC surface analysis at 2100 UTC[5], which is the time NHC considered Sandy to have become extratropical and about 2.5 hours before landfall. Note the inverted frontal wave structure, with the warm front pushing westward and the cold and occluded fronts pushing northward. Further illustrating that extratropical transition is well underway is the GOES 2345 UTC water vapor image shown in Fig. 4a. Three key airstreams associated with well-developed extratropical cyclones (Fig. 4b, adapted from Raven-Rubin and Wernli (2015)) are all evident in the water vapor image: the warm conveyor belt (pink), the cold conveyor belt (blue), and the descending dry air intrusion (yellow).

b. Late stage extratropical transition

Tropical cyclones that undergo extratropical transition prior to landfall present forecasting challenges (DiMego and Bosart 1982, Jones et al. 2003, Milrad et al. 2013). The late stage of Sandy's ET is exemplified in radar reflectivity by the rapid symmetry destruction in Sandy before landfall. Figure 5 shows the DIX WSR-88D radar reflectivity for 305 meter constant altitude at

---

[5] Wherever times are shown without a date, they refer to the period 0500 UTC 29 October 2012 through 0100 UTC 30 October 2012.

2238 UTC, where the yellow and green arc in the southwest quadrant is deep convection ahead of the southwest-ward advancing warm front. The blue and green swath in the center is shallow precipitation within warm, moist air and the light blue arc along the coast is the leading edge of the cool intrusion. A pair of low level jets (LLJ) over New Jersey (discussed below) appears to play a role in the symmetry destruction, as supported by the simulation and surface observation data. In 3 hours (1800 to 2100 UTC) a northeasterly warm, moist, maritime-sourced LLJ transforms circular rain-bands near Sandy's core into a northwestward arc as an intensifying warm front (Fig. S-2). An easterly cooler, continental-sourced LLJ plunges westward into the northern New Jersey coast at 2230 UTC, sweeps westward across New Jersey through 0000 UTC, and stretches the remaining convection bands westward even further. Timing of the above is consistent with regional average time series of observed surface wind speeds and temperatures (section 4a below) and with the storm core's traversal of cool coastal shelf water.

Encirclement of Sandy's core by cooler, drier air is shown in Fig. 6 for the simulation at 2200 UTC, although location and timing of specific features differ somewhat from the observed radar reflectivity of Fig. 5 at 2238 UTC. The image at the earth's surface is colored by the simulation's 2 meter temperature and the 3-D iso-surface encloses higher-concentration water vapor. Iso-surface colors denote elevation, with red and yellow below 1 km. This illustrates how warm, moist air was etched away from the east and above by cooler, drier air. A time-animated potential temperature iso-surface (Fig. S-3) illustrates this more clearly.

Additional visualizations (Fig. S-4) illustrate that offshore-flowing cold air is modified by the elevated sea surface temperature as air circulates eastward and then northward around the southern and eastern sectors of the storm. As the storm center nears the coastline after 2200 UTC, the over-water trajectory of offshore-flowing cold air diminishes significantly in length, thus affording a briefer opportunity for the warm sea surface to modify the air. Thus, encirclement of the storm center by cold air has the appearance of accelerating as the storm center nears the coastline. The encirclement acceleration is amplified as the trajectory of the cold air becomes southerly over the cooler sea surface west of the Gulf Stream as the storm center nears the coastline.

c. Low level jets and airstreams

The 3-dimensional structure of low level jets and airstreams can be seen in Fig. 7 (time animated in Fig. S-5), which shows the 3-D iso-surface that encloses simulated wind speeds that exceed 34 m s^{-1}. Iso-surface color indicates elevation, where red and orange are below 1 km, and blue is above 5 km. Referring to the sketch in Fig. 4b, the easterly green wedge north of the storm center in Fig. 7 corresponds to the warm conveyor belt, the westerly green wedge south of the storm center corresponds to the cold conveyor belt, and the northerly blue wedge east

of the storm center (truncated at is southern edge by the domain wall) corresponds to the descending dry air intrusion.

WRF 3-D wind speed fields show that these LLJs traversed the region from 1800 through 0000 UTC. The southern jet's intensity appears to be overdone in the simulation between at least 1400 to 2200 UTC during which the surface jet spans a buoy. These LLJs appear to be spiraling around an axis parallel to the surface, as exhibited by simulated wind fields. In profile, the simulation exhibits a wind speed increase from 10 to 1,250 meters elevation, which is consistent with the OKX rawinsonde wind profile at 0000 UTC. At that time the highest simulated wind speeds are at 1 km elevation over the middle Chesapeake Bay and at or above 3.4 km over the Hudson River. Maximum radar winds above Fort Dix, NJ are 50 m s^{-1} between 1.1 and 1.9 km during 1742 to 2022 UTC, which is consistent with both the simulation and the 1800 UTC OKX rawinsonde profile. The relationship of these jets and airstreams to the larger scale environment of Hurricane Sandy is discussed by Shin and Zhang (2017).

d. Frontal zones and air masses

The most significant frontal boundary associated with Sandy arcs inward from northwest of the storm center to south of the center, as evident in Figs. 3, 5 and 6. This frontal zone is evident in the simulation from 1800 UTC 28 October and persists after landfall through 0300 UTC 30 October, after which it appears to decay near the upper Chesapeake Bay. The zone spirals closer to the storm center as time progresses and its linear dimension shrinks with time from about 1,000 km at 1800 UTC 28 October to 300 km at 0300 UTC 30 October. The frontal zone arc maintains a northwest-to-southeast orientation throughout its duration, however.

The frontal zone's intensity is manifested in the simulation (Fig. S-6) at the surface by strong horizontal temperature and wind speed gradients and by significant convergence of horizontal streamlines. There also appears to be a wind lull about 10-40 km wide on the warm side of the convergence zone. The simulated frontal zone is extremely narrow, estimated to be about 4 km wide. With a horizontal temperature difference of about 2 K across the frontal zone, the zone's temperature gradient is estimated from the simulation to be about 0.5 K/km.

The air mass behind the warm front is manifested in observations as a warm intrusion that enters New Jersey during 1500 UTC to 2200 UTC driven by north-northeasterly winds, as exhibited by surface observations and radar base velocity fields. Temperatures begin to both warm (0900 UTC) and cool (2200 UTC) earlier along the coast compared to inland (1400 and 0000 UTC, respectively), indicative of the westward intrusion of both warm and cool air as seen on regional average temperature time series discussed in section 4a. Warming of 4-6 degrees K that occurs along and north of the storm track is not experienced south of track, although cooling accelerates south of track around 0000 UTC as seen on regional average temperature time series. The warm front does not progress southward beyond about 50 km south of track.

The cool intrusion is exhibited in wind profile observations which suggest that the leading edge of the southern cooler, drier LLJ that encircled the storm center advanced faster aloft over northern New Jersey, destabilizing the boundary layer there. The implication of this is discussed in the Supplement's section S-4.

The simulated impact of warmer coastal estuary water on modifying the offshore-flowing cold air mass apparently reaches hundreds of kilometers offshore (Fig. S-4). The effect is most apparent for the largest estuary, the Chesapeake Bay, but is also evident for the Pamlico and Albemarle Sounds. The offshore airflow is southeastward and eastward out of the estuaries south of the storm center and the effect is exhibited by narrow arcs of enhanced surface temperature. The offshore reach is as far as 600 km from the mouth of the bay. Interestingly, surface temperature contours reflect the coastline shape, albeit somewhat distorted by the significant radial variation in wind speed southwestward from the storm center.

e. Offshore high-speed surface wind dart

The WRF simulation exhibits an oceanic "dart" (Shapiro et al. 2013) of warm, high-speed wind (Fig. 8a and animated in Fig. S-7) which progresses toward the west-southwest during 0700 through 1000 UTC. Whether it actually occurred is unknown because of scarcity of oceanic observations. It does appear to be the entity that leads the warm intrusion into New Jersey, whose leading edge reaches the northern New Jersey coast at 1330 UTC. This fast-moving, arrow-shaped, surface-based wind jet darts from northeast of the storm center at 0500 UTC to northwest of the center by 0900 UTC. During those 4 hours the tip of the dart travels 430 km, yielding a propagation speed of about 30 m s^{-1}. The dart is characterized by sharp wind speed boundaries on both its northern and southern edges, has its highest wind speeds on its southern edge, and embodies warmer air than its surroundings, as observed by temperature contours in Fig. 8a.

The higher simulated surface temperature inside the dart is emphasized in Fig. 8b, which exaggerates the temperature color range in its vicinity. Note that radial gradients (with respect to storm center) of temperature within and outside the dart are comparable, but higher surface temperature within it is displaced northward (outward from storm center) compared to its surroundings.

Other visualizations (Fig. S-8) suggest that warmer, dryer, faster air is transported downward on the left (southern) edge of the dart while upward motion on its right (northern) edge appears to undercut the cooler air into which the dart is advancing. This suggests that the simulated dart's flow is comprised of a conical left-hand spiral pointing and propagating toward the west-southwest, where the dart's point represents the cone apex.

The visualizations also suggest that the warm wind dart concentrates the surface temperature gradient from a broad area to a narrow arc, which, by 1230 UTC becomes coincident with the strong frontal zone, thus further strengthening the frontal zone. There appears to be a void in simulated convection at the dart's southern edge, which is consistent with downward motion there.

The simulated surface manifestation of the dart appears to be a small downward-reaching extremity of an easterly jet on the northern sector of the storm, where the downward extremity propagates inward (southward) with time along the core of the jet, from the outer (northern) edge of its core at 0500 UTC to the inner (southern) edge at 0830 UTC. There is a local minimum in wind speed at the northern edge of the dart which extends to an elevation of at least 1 km. The potential temperature enhancement within the dart also appears to extend to an elevation of at least 1 km.

4. Observed winds and WRF comparisons

Analyses of observed and simulated variables (mainly wind speed) reported herein comprise two categories: (1) distributions, which are over time (time series in section 4a), geography (maps in section 4b) and occurrence probability (histograms in section 4c) and (2) summary statistics (tables in section 4d), which include maximum wind speed, time of maximum speed and mean speed.

a. Time series

Time series of observed and simulated winds were produced for all 126 surface observation stations in the data set, spanning the 72 hour time range of 0000 UTC October 28 through 0000 UTC October 31, with WRF data limited to a 36 hour span beginning at 0000 UTC October 29. Time resolution is 5 minutes for most surface observation stations and 30 minutes for WRF output. To compare values of observed with WRF variables, the value of the WRF variable at the grid point nearest the observation station was used.

Examining the observed wind speed time series plots for the entire set of 126 stations (not shown), two major characteristics stand out: (1) plots vary considerably in character and magnitude among sites, even among neighboring sites and (2) temporal variability is much greater in observed than simulated wind speeds. That is, observation time series are more feature-rich than WRF's, on a multi-hour time scale. For example, the rise and fall of wind speed bracketing landfall time is much more peaked in observations than WRF. This behavior is common for many stations. The muted multi-hour variability of WRF wind speed time series might be at least partially due to the dependence of the WRF wind speed bias on wind speed noted by Frediani et al. (2016), discussed further in section 4c.

To explore regional differences in time series, the landfall area was divided regionally and time series of mean surface wind and temperature within each region were plotted for each region. There are 6 overland regions and 4 overwater regions. Overland regions are divided east-west into coastal and interior locales and north-south into (1) north-of, (2) along and (3) south-of locales relative to storm track. Overwater regions are coastal oceanic, open oceanic, Delaware Bay and Long Island Sound. The two oceanic regions are much more data-sparse than the other 8 regions.

Regionally averaged time series of surface wind speed and temperature are shown in Fig. 9 for the 6 overland regions, where blue lines are wind speed and red lines are temperature. Any observed wind speeds not measured at the 10 meter elevation are adjusted per the method described in the Supplement's section S-2. No adjustment is made for elevation of temperature observation. WRF surface variables represent wind speed at 10 meter and temperature at 2 meter elevations. Nominal landfall time is at 0000 UTC on October 30 as denoted by the heavier vertical line at that time. The larger variability of wind speed observations compared to WRF on a multi-hour time scale is even exhibited in the regionally averaged time series of Fig. 9. Note that observed wind speeds exceed simulated speeds only in the north coastal region during about 3 hours around landfall time. Note also that observed temperature for regions along or north of track peaks before landfall in coastal regions but around landfall time in interior regions. These latter features are discussed in sections 4b, 4d and 5.

b. Geographical distributions

The geographical distribution of observed and simulated surface winds across the landfall region was studied by producing maps showing wind barbs at station sites, supplemented by shaded contour images of wind speed, interpolated from wind speeds at stations. Separate maps are shown in Fig. 10 for maximum wind speed, time of maximum speed and mean speed. Maximum wind speeds are obtained for the *5 minute sample* observations rather than for the *5 minute maximum speed* observations, to allow a more relevant comparison with WRF surface wind speeds. Analogous maps were produced for simulated winds (Fig. 11). Only stations whose observations persisted until at least 0200 UTC October 30, two hours after landfall time, are included in the maps. For maximum wind speeds, the search for maxima begins at 1200 UTC October 29. For mean wind speeds, only observations in the 4 hour window symmetrically bracketing landfall time are included, because of the large site-to-site variability of time series shapes beyond the narrow landfall period, as mentioned above in section 4a. Barbs show direction and speed of maximum and mean winds on their respective maps.

Figure 10b shows that maximum observed wind speeds occurred over New Jersey coastal extremities: south of Sandy Hook and near Cape May. These maximum speeds along the coast were most subdued near the landfall site, where maxima occurred 2 to 4 hours before landfall.

Figure 10a shows that maximum wind speeds along the coast occurred *before* landfall along the track and far north and south of track, and *after* landfall immediately north and south of track, yielding an alternating pattern centered on the landfall site.

Highest WRF wind speeds occurred over the Delaware Bay near its mouth and offshore from its mouth. WRF wind speed vertical profiles show that wind speeds are higher south of the storm track at all elevations from 10 to 1,250 m. Maximum WRF wind speeds along the coast were most subdued south of the landfall location and south of Sandy Hook. Earliest maximum WRF winds occurred from the landfall site northward and southwest of the Delaware Bay.

Two stations have early maxima embedded within a broader region of late maxima in the southwestern quadrant of Fig. 10a. The two stations are Clayton, NJ and Viola, DE. Their time series plots and those of their nearest neighbors indicate that at Clayton the wind speed trace has high short-term variability and there happens to be a spike in wind speed near 1200 UTC that is slightly higher than the later multiple peaks that occur just before 0000 UTC. At Viola, the wind speed traces differ much among Viola and those neighboring it, with at least three broad peaks evident at all sites. It happens that the peak at Viola near 1400 UTC is higher and broader than the later peak after landfall near 0600 UTC.

Figure 10c shows that average observed wind speeds during 4 hours bracketing landfall time exhibit banding that is roughly parallel to the storm track. Stripes of high winds occur 50 km north and south of the track, where the southern stripe is mostly over the Delaware Bay. Stripes of low winds are along the track, south of the southern coast of the Delaware Bay, and across far northern New Jersey.

Average WRF wind speeds during 4 hours bracketing landfall time exhibit banding similar to the observed winds, although the wind speed range among stripes is much more muted. The stripes of high winds 50 km north and south of the track exhibit higher predicted wind speeds than observed near the coastlines. The stripes of low winds along the track, south of the southern coast of the Delaware Bay, and across far northern New Jersey, exhibit higher predicted wind speeds than observed.

Main contrasts between observed and simulated winds are that (1) observed maximum winds south of Sandy Hook is not reflected in WRF winds, (2) observed (WRF) winds are more intense on the right (left) side of the track and (3) early timing (4-6 hours before landfall) of maximum WRF winds over the New York City metropolitan region and most of Delaware is not reflected in observations.

c. Probability distributions

Probability density distributions were produced for observed and simulated surface wind speeds during the 12 hour period 1400 UTC October 29 to 0200 UTC October 30. Separate distributions were produced for 79 overland sites (Fig. 12a) and 7 overwater sites (Fig. 12b). Delaware Bay water sites were excluded from the overwater distributions because (1) a northwest-southeast line of high wind speed gradient was aligned along the middle of the bay throughout the period and (2) many bay sites were near shore and likely affected by off-land fetches.

Over *land*, WRF has a much narrower wind speed distribution compared to the observed distribution, with the width of the middle 80% of the distribution (10-90 percentile range) being 8 and 14 m s^{-1} for WRF and observations, respectively. This difference is likely due to WRF's known bias of predicting higher wind speeds over plains and valleys (Jimenez and Dudhia 2012), where most stations reside and over land in general for WRF (Draxl et al. 2010, Yang et al. 2017), even for WRF-LES (Talbot et al. 2012). Over *water*, the middle 80% of the distribution is 13 and 11 m s^{-1} for WRF and observations, respectively. That the distribution widths are more similar over water is consistent with the absence over water of a bias analogous to that described above for land sites. This WRF wind speed bias is discussed more fully in section 5b.

d. Spatiotemporally averaged wind speeds

Spatiotemporally averaged observed and simulated surface wind speeds were calculated for the 4 hour period bracketing landfall time of 0000 UTC October 30 for 10 different regions, which are the same 10 regions described in section 4a. All observations are for 5 minute samples and only stations whose observations persisted until at least 0200 UTC October 30, two hours after landfall, are included. Surface wind speed results are shown in Table 3a for observations, 3b for simulations and 3c for ratios of simulated to observed wind speeds.

As shown in Tables 3a and 3b, highest mean wind speeds during the 4 hour landfall period for both observations and WRF occurred over the coastal ocean region. Over land, highest mean wind speeds from observations (WRF) occurred over the north (south) coastal region.

As evident in Table 3c, it is of interest that WRF *under*-predicted wind speeds in regions neighboring New York City, such as the north coastal region, Long Island Sound and the western ocean region, because this discrepancy is similar to that of storm surge forecasts for post-tropical cyclone Sandy (Forbes et al. 2014). WRF over-predicted wind speeds everywhere else, including by 34 to 61% over interior regions, an over-prediction bias over land that is noted by others (Draxl et al. 2010, Mass and Ovens 2010, Talbot et al. 2012, Zhu 2008) and by 28% over the Delaware Bay and the neighboring south coastal region. WRF also over-predicted by more than double near the storm track along the coast. This large discrepancy is due to WRF's

predicting an eye size that is much smaller than observed. A similar left-of-track WRF over-prediction of wind speed was noted for Hurricane Isabel (2003) by Lin et al. (2010).

5. Discussion

This section discusses the impact of (a) LECs and (b) physiographic features on surface winds.

a. Impact of large eddy circulations on wind

Signatures of LECs are evident in this analysis of radar and surface observations and WRF output during Sandy's landfall. They are evident in radar reflectivity and velocity plan position indicator (PPI) images, and possibly in observed surface wind speed time series. In addition, the 500 meter resolution WRF simulation using the YSU PBL scheme appears to resolve LECs and exhibits signatures similar to observations. The extent of the analysis is limited, however, by the temporal resolution of both observations (5 minutes) and simulation output (30 minutes).

In radar radial velocity (Fig. 13a) and reflectivity (Fig. 5) PPI images, signatures aligned parallel to the east-northeasterly flow are most evident over northwestern New Jersey during 1800 to 2100 UTC. They are even more clearly evident in time animations of radial velocity (Fig. S-9) and reflectivity (Fig. S-2). Signatures abruptly change alignment to WNW-ESE at 2300 UTC. Their wavelengths are about 8 km, horizontal extent of signature patterns are roughly 40 km and signatures propagate toward west-northwest at a rate of about one wavelength per 2-3 radar frames (11-17 minutes). A time series segment of the 5 minute maximum wind speed at Andover, NJ exhibits a 15 minute periodicity during 2000 to 2100 UTC (Fig. 13b), which is consistent with the feature propagation speed observed on radar.

There also are radar and simulation signatures aligned perpendicular to the northwesterly flow over southwestern New Jersey during 0000 to 0100 UTC. These are smaller than those over northwestern New Jersey, with wavelengths of about 4 km and horizontal extents of roughly 20 km.

The simulation exhibits characteristics similar to those seen on radar PPI images, which can be seen in time-animated maps of simulated reflectivity (Fig. S-10a) and vertical velocity (Fig. S-10b) imagery. Furthermore, the simulation vertical cross sections through LECs exhibit characteristics that are similar to those simulated by others (Gao and Ginis 2016, Green and Zhang 2015a, Nakanishi and Niino 2012, Zhu 2008) in storm-tangential wind speed characteristics, in radial circulation characteristics and of wavelengths, as illustrated in Figs. 14a and 14b for this WRF simulation and the LES of Nakanishi and Niino 2012, respectively.

b. Impact of physiographic features on WRF winds

Surface winds predicted by WRF exhibit a significant dependence on location. To aid in interpreting this dependence, a description of the WRF model entities that quantify surface

winds is presented in the Supplement's section S-5. To accentuate the impact of geographical features on WRF surface wind speed, wind speed fields are averaged over the 4 hour period bracketing landfall time of 0000 UTC for each grid point and displayed in Fig. 15a. Animations of discrete 30-minute interval WRF surface wind speed fields (Fig. S-11) illustrate this even more clearly, in that some features move and evolve with time but others remain fixed to locations. These features include coastlines, inland lakes and rivers, urban regions, and land cover types. This impact arises from the quantized categorization of land use in WRF, the large roughness length (z_0) differences among land use categories and the 10 meter wind speed dependence on z_0, as described in the Supplement's section S-5 and demonstrated by Eq. (4) therein.

To illustrate the impact further, a map displaying land surface roughness values used in the simulation is shown in Fig. 15b. Values of z_0 are from the WRF Preprocessing System (WPS) default static data set containing the USGS 24-category land use categories (Wang et al. 2012). The 1000x1000 grid point WRF geographical domain subset used herein contains only 8 unique categories of land use of the 24 possible categories and over land, only 4 different values of z_0 are encountered: 5, 20, 50 and 80 cm. Values of z_0 of 20 and 50 cm dominate the domain area-wide, but values of 5 and 80 cm, the overland extremes that represent crop and urban land, respectively, often occur in adjacent regions. This is manifested in surface wind speed fields of Fig. 15a as wind speed local minima over rougher terrain and local maxima over smoother terrain. Such land roughness dependence is evident in geography-fixed features reported by others (Talbot et al. 2012). The dramatic drop-off in WRF surface wind speeds at coastlines is also noted by others (Zhu 2008), although effects other than surface roughness may also be contributing (Green et al. 2011).

Particularly striking features of this type are wind speed local maxima over inland water bodies. This impact is most evident on horizontal profiles of wind speed shown in Fig. 16. Figure 16a shows WRF wind speed at 4 elevations along the SSW-NNE blue line shown in Fig. 15. Figure 16b shows the ratio of wind speed at 10 meters to wind speed at 3 higher elevations: 202, 664 and 1,248 meters (approximate middle of model layers 3, 6 and 11, respectively). Figure 16b also shows a plot of $a - \ln(z_0)$ which is arbitrarily scaled for qualitative comparison with the wind speed horizontal profiles and is inverted to represent smoothest terrain upward. Note how well this inverted roughness length profile tracks wind speed ratios at all 3 levels, even to the extent that the gradual decrease in roughness (increase in smoothness) from 39.5 to 39.8 degrees latitude is reflected in the wind speed ratio profiles.

This analysis demonstrates (1) the extent to which WRF's surface wind speed predictions depend on z_0 and (2) the need for using better and higher resolution land use data to improve surface wind speed predictions. But it is first necessary to know how *much* of this dependency

is borne out in actual observations. Further quantification of this extent, by comparison with observations, will be addressed in follow-on work.

The most extensive roughness length boundary is, of course, the coastline. Streaks of lower (higher) simulated surface wind speeds over water (land) are evident downwind of terrain (estuary) features and these streaks slowly evolve in orientation and shape as wind direction evolves. These effects reach depths of at least 700 meters near significant features. For example, when air flow is parallel to Long Island and its Sound during 1500 to 1900 UTC, streaks of diminished and enhanced winds extend downwind from those geophysical features into northern New Jersey as illustrated by the animation of the 202 meter elevation wind speed shown in Fig. S-12.

In observations, the coastline effect is most obvious at Lewis, DE. A very large horizontal wind speed gradient exists within the Delaware Bay along a frontal boundary therein at 1900 UTC, where wind speed immediately south of the boundary is double that north of it. Wind direction backs at Lewis, DE, from bay to land during a rapid speed drop-off spanning 0000 UTC as exhibited also by WRF. Observed wind direction at Lewis backs to 270° at 2330 UTC, which rapidly diminishes the over-water fetch to almost zero at that time. Although wind speed begins dropping by 2315 UTC, the most rapid drop-off is after 2330 UTC.

Besides roughness length, there is some evidence of a dependence of WRF simulated surface wind speed on terrain elevation. Station-mean ratios of simulated to observed surface wind speeds show that many stations at higher elevations have low ratios: 5 of the 20 highest elevation stations are also ranked among the 20 most under-predicted wind speeds and found to be located on top of mountains, plateaus or hills. This behavior is consistent with a known WRF bias of under-predicting wind speeds over hills, ridges and mountains (Jimenez and Dudhia 2012).

6. Summary

Highlights of this work's results are:

- Various aspects of observed surface wind fields during Sandy's landfall on New Jersey were characterized. Highest observed winds occurred over New Jersey coastal extremities, with a primary maximum south of Sandy Hook and a secondary near Cape May.
- Storm structural mechanisms that drove surface wind fields were interpreted using the WRF simulation and radar and rawinsonde observations. WRF surface winds are driven mainly by two LLJs: an easterly warm jet north of the storm center and a westerly cool

LLJ south of the center. A strong frontal zone and warm and cool air masses also played key roles.

- Wind speed observations were compared with WRF predictions. WRF over-predicts regionally-averaged wind speeds at all land locations and times except for the northern coastal region during and after landfall. This land-based over-prediction is consistent with a known WRF bias.

- Large eddy circulation signatures were characterized using radar and surface observations and the WRF simulation. Signatures appear over northern New Jersey and Pennsylvania throughout the landfall period, have wavelengths of about 8 km and propagate toward the west-northwest. Signature characteristics are similar to those of recent HBL LES studies reported by others (Gao and Ginis 2016, Green and Zhang 2015a, Green and Zhang 2015b, Nakanishi and Niino 2012, Zhu 2008).

- The fine spatial variation of surface wind fields predicted by the high resolution WRF simulation was demonstrated to depend on land use categories. The WRF surface winds exhibit features of various scales, some of which move with storm flow and some of which are tied to geographical features. The geography-tied features arise from quantized roughness lengths of land use.

- Opportunities to improve predictions of surface wind fields during land-falling tropical cyclones were identified. These include using (1) finer resolution land surface roughness fields (Talbot et al. 2012, Jimenez and Dudhia 2012), (2) explicit inclusion of topographic roughness (Jimenez and Dudhia 2012) and (3) better HBL turbulence parameterizations to represent vertical transport by LECs (Jimenez et al. 2012).

- Results illustrate the importance of understanding and predicting the fine structure of surface wind fields as input to inundation models, in particular, of LECs, frontal zones and their evolution, mesoscale intense wind streaks and land surface and topographic roughness influences. Such knowledge is also important for forecasting wind farm energy production (Draxl et al. 2010, Worsnop 2016).

Acknowledgements

helpful insights and references on inundation forecasting and to Michael Splitt for similar contributions on observed wind speed adjustments.

References

Alves, J.-H. G. M., S. Stripling, A. Chawla, H. Tolman, and A. van der Westhuysen, 2015: Operational Wave Guidance at the U.S. National Weather Service during Tropical/Post–Tropical Storm Sandy, October 2012. *Mon. Wea. Rev.*, **143**, 1687–1702.

Balzarini, A., F. Angelini, L. Ferrero, M. Moscatelli, M. G. Perrone, G. Pirovano, G. M. Riva, G. Sangiorgi, A. M. Toppetti, G. P. Gobbi, and E. Bolzacchini, 2014: Sensitivity analysis of PBL schemes by comparing WRF model and experimental data. *Geosci. Model Dev. Discuss.*, 7, 6133–6171.

Bassill, N. P., 2014: Accuracy of early GFS and ECMWF Sandy (2012) track forecasts: Evidence for a dependence on cumulus parameterization, *Geophys. Res. Lett.*, **41**, 3274–3281, doi:10.1002/2014GL059839.

Blake, E. S., T. B. Kimberlain, R. J. Berg, J. P. Cangialosi, and J. L. Beven III, 2013: Tropical Cyclone Report: Hurricane Sandy (AL182012). Tech. Rep. AL182012, NOAA/National Hurricane Center, 157 pp.

Blumberg, A.F., N. Georgas, L. Yin, T. O. Herrington, and P. M. Orton, 2015: Street-Scale Modeling of Storm Surge Inundation along the New Jersey Hudson River Waterfront. *J. Atmos. Oceanic Technol.*, **32**, 1486–1497, doi: 10.1175/JTECH-D-14-00213.1.

Bosart, L. F., 2013: Hurricane Sandy (2012): A Multiscale Analysis and Perspective. *16th Cyclone Workshop,* Sainte-Adèle, Quebec, Canada, 22-27 September 2013.

Bowyer, P.J. and A.W. MacAfee, 2005: The Theory of Trapped-Fetch Waves with Tropical Cyclones—An Operational Perspective. *Wea. Forecasting*, **20**, 229–244, doi: 10.1175/WAF849.1

Braun, S. and W. Tao, 2000: Sensitivity of High-Resolution Simulations of Hurricane Bob (1991) to Planetary Boundary Layer Parameterizations. *Mon. Wea. Rev.*, **128**, 3941–3961, doi: 10.1175/1520-0493(2000)129<3941:SOHRSO>2.0.CO;2.

Bretherton, C. S., and S. Park, 2009: A New Moist Turbulence Parameterization in the Community Atmosphere Model. *J. Climate*, **22**, 3422–3448.

Bryan, G. H., R. P. Worsnop, J. K. Lundquist, and J. A. Zhang, 2017: A Simple Method for Simulating Wind Profiles in the Boundary Layer of Tropical Cyclones. *Bound.-Layer Meteor.*, **162**, 475–502.

Businger, J., J. Wyngaard, Y. Izumi, and E. Bradley, 1971: Flux-Profile Relationships in the Atmospheric Surface Layer. *J. Atmos. Sci.*, **28**, 181–189, doi: 10.1175/1520-0469(1971)028<0181:FPRITA>2.0.CO;2.

Cheng, W. and W. Steenburgh, 2005: Evaluation of Surface Sensible Weather Forecasts by the WRF and the Eta Models over the Western United States. *Wea. Forecasting*, **20**, 812–821, doi: 10.1175/WAF885.1.

Chourasia, A., M. Wong, D. Mishin, D. R. Nadeau, and M. Norman, 2016: SeedMe: A scientific data sharing and collaboration platform. In Proceedings of the XSEDE16 Conference on Diversity, Big Data, and Science at Scale (XSEDE16). ACM, New York, NY, USA, Article 48, 6 pages. DOI=10.1145/2949550.2949590

Clyne, J., Mininni, P., Norton, A., and Rast, M., 2007: Interactive desktop analysis of high resolution simulations: application to turbulent plume dynamics and current sheet formation. *New J. Physics*, **9**, 301.

Cohen, A. E., S. M. Cavallo, M. C. Coniglio, H. E. Brooks, 2015: A Review of Planetary Boundary Layer Parameterization Schemes and Their Sensitivity in Simulating Southeastern U.S. Cold Season Severe Weather Environments. *Wea. Forecasting,* **30**, 591–612.

Davis, C., W. Wang, S. S. Chen, Y. Chen, K. Corbosiero, M. DeMaria, J. Dudhia, G. Holland, J. Klemp, J. Michalakes, H. Reeves, R. Rotunno, C. Snyder, and Q Xiao, 2008: Prediction of Landfalling Hurricanes with the Advanced Hurricane WRF Model. *Mon. Wea. Rev.*, **136**, 1990–2005.

DiMego, G. J., and L. F. Bosart, 1982: The Transformation of Tropical Storm Agnes into an Extratropical Cyclone. Part I: The Observed Fields and Vertical Motion Computations. *Mon. Wea. Rev.*, **110**, 412–433.

Draxl, C., A. N. Hahmann, A. Pena Diaz, J. N. Nissen, and G. Giebel, 2010: Validation of boundary-layer winds from WRF mesoscale forecasts with applications to wind energy forecasting. 19th Symposium on Boundary Layers and Turbulence 2010 Jan 1.

Drews, C. and T. J. Galarneau, 2015: Directional Analysis of the Storm Surge from Hurricane Sandy 2012, with Applications to Charleston, New Orleans, and the Philippines. *PLoS ONE*, **10**, (3): e0122113. doi:10.1371/journal.pone.0122113.

Evans, C., K. Wood, S. Aberson, H. Archambault, S. Milrad, L. Bosart, K. Corbosiero, C. Davis, J. Dias Pinto, J. Doyle, C. Fogarty, T. Galarneau, Jr., C. Grams, K. Griffin, J. Gyakum, R. Hart, N. Kitabatake, H. Lentink, R. McTaggart-Cowan, W. Perrie, J. Quinting, C. Reynolds, M. Riemer, E. Ritchie, Y. Sun, and F. Zhang, 2017: The Extratropical Transition of Tropical Cyclones. Part I: Cyclone Evolution and Direct Impacts. *Mon. Wea. Rev.* doi:10.1175/MWR-D-17-0027.1, in press.

Forbes, C., J. Rhome, C. Mattocks, and A. Ta, 2014: Predicting the Storm Surge Threat of Hurricane Sandy with the National Weather Service SLOSH Model. *J. Mar. Sci. Eng.*, **2**, 437-476, doi:10.3390/jmse2020437.

Foster, R. C., 2005: Why Rolls are Prevalent in the Hurricane Boundary Layer. *J. Atmos. Sci.*, **62**, 2647-2661.

Franklin, J. L., M. L. Black, and K. Valde, 2003: GPS Dropwindsonde Wind Profiles in Hurricanes and Their Operational Implications. *Wea. Forecasting,* **18**, 32–44.

Frediani , M. E. B., J. P. Hacker, E. N. Anagnostou, and T. Hopson, 2016: Evaluation of PBL Parameterizations for Modeling Surface Wind Speed during Storms in the Northeast United States. *Wea. Forecasting*, **31**, 1511–1528, doi: 10.1175/WAF-D-15-0139.1.

Galarneau, T. J., C. A. Davis, and M. A. Shapiro, 2013: Intensification of Hurricane Sandy (2012) through extratropical warm core seclusion. *Mon. Wea. Rev.*, **141**, 4296–4321, doi:10.1175/MWR-D-13-00181.1.

Gall, R., J. Tuttle, and P. Hildebrand, 1998: Small-Scale Spiral Bands Observed in Hurricanes Andrew, Hugo, and Erin. *Mon. Wea. Rev.*, **126**, 1749–1766, doi: 10.1175/1520-0493(1998)126<1749:SSSBOI>2.0.CO;2.

Gao, K. and I. Ginis, 2016: On the Equilibrium-State Roll Vortices and Their Effects in the Hurricane Boundary Layer. *J. Atmos. Sci*., **73**, 1205–1222, doi: 10.1175/JAS-D-15-0089.1.

Gao, Z., Wang, Q., and Zhou, M., 2009: Wave-Dependence of Friction Velocity, Roughness Length, and Drag Coefficient over Coastal and Open Water Surfaces by Using Three Databases. *Adv. Atmos. Sci.*, **26**, 5, 887-894.

Good, S. P., D. V. Mallia, J. C. Lin, and G. J. Bowen, 2014: Stable Isotope Analysis of Precipitation Samples Obtained via Crowdsourcing Reveals the Spatiotemporal Evolution of Superstorm Sandy. *PLoS ONE*, **9**, e91117.

Gopalakrishnan, S., F. Marks, J. Zhang, X. Zhang, J. Bao, and V. Tallapragada, 2013: A Study of the Impacts of Vertical Diffusion on the Structure and Intensity of the Tropical Cyclones Using the High-Resolution HWRF System. *J. Atmos. Sci.*, **70**, 524–541, doi: 10.1175/JAS-D-11-0340.1.

Green, B. W. and F. Zhang, 2015a: Idealized Large-Eddy Simulations of a Tropical Cyclone-like Boundary Layer. *J. Atmos. Sci.*, **72**, 1743-1764.

Green, B. W. and F. Zhang, 2015b: Numerical simulations of Hurricane Katrina (2005) in the turbulent gray zone, *J. Adv. Model. Earth Syst*., **7**, 142–161, doi: 10.1002/2014MS000399.

Green, B., F. Zhang, and P. Markowski, 2011: Multiscale Processes Leading to Supercells in the Landfalling Outer Rainbands of Hurricane Katrina (2005). *Wea. Forecasting*, **26**, 828–847, doi: 10.1175/WAF-D-10-05049.1.

Greene, C.H., J. A. Francis, and B. C. Monger, 2013: Superstorm Sandy: A series of unfortunate events? *Oceanography*, **26**, 8–9, http://dx.doi.org/10.5670/oceanog.2013.11.

Grenier, H. and C. S. Bretherton, 2001: A Moist PBL Parameterization for Large-Scale Models and Its Application to Subtropical Cloud-Topped Marine Boundary Layers. *Mon. Wea. Rev.*, **129**, 357–377.

Hewson, T., 2015: Cyclonic Windstorms – Morphology, Predictability and Model Representation. Fifth Workshop on European Storms, Bern, Switzerland. August 31, 2015.

Hill, K. and G. Lackmann, 2009: Analysis of Idealized Tropical Cyclone Simulations Using the Weather Research and Forecasting Model: Sensitivity to Turbulence Parameterization and Grid Spacing. *Mon. Wea. Rev.*, **137**, 745–765, doi: 10.1175/2008MWR2220.1.

Hong, S.-Y., Y. Noh, J. Dudhia, 2006: A New Vertical Diffusion Package with an Explicit Treatment of Entrainment Processes. *Mon. Wea. Rev.*, **134**, 2318–2341.

Ito, J., T. Oizumi, and H. Niino, 2016: Large Eddy Simulation on Entire Tropical Cyclones. 32nd AMS Conference on Hurricanes, April 20, 2016.

Janjic, Z. I., 1994: The step-mountain eta coordinate model: Further developments of the convection, viscous sublayer, and turbulence closure schemes. *Mon. Wea. Rev.*, **122**, 927–945.

Jimenez, P. and J. Dudhia, 2012: Improving the Representation of Resolved and Unresolved Topographic Effects on Surface Wind in the WRF Model. *J. Appl. Meteor. Climatol.*, **51**, 300–316, doi: 10.1175/JAMC-D-11-084.1.

Jimenez, P., J. Dudhia, J. González-Rouco, J. Navarro, J. Montávez, and E. García-Bustamante, 2012: A Revised Scheme for the WRF Surface Layer Formulation. *Mon. Wea. Rev.*, **140**, 898–918, doi: 10.1175/MWR-D-11-00056.1.

Johnsen, P., M. Straka, M. Shapiro, A. Norton, and T. Galarneau, 2013: Petascale WRF Simulation of Hurricane Sandy: Deployment of NCSA's Cray XE6 Blue Waters. SC13, International Conference for High Performance Computing, Networking, Storage and Analysis, Denver, CO, USA — November 17-21, 2013.

Jones, S., P. Harr, J. Abraham, L. Bosart, P. Bowyer, J. Evans, D. Hanley, B. Hanstrum, R. Hart, F. Lalaurette, M. Sinclair, R. Smith, and C. Thorncroft, 2003: The Extratropical Transition of Tropical Cyclones: Forecast Challenges, Current Understanding, and Future Directions. *Wea. Forecasting*, **18**, 1052–1092, doi: 10.1175/1520-0434(2003)018<1052:TETOTC>2.0.CO;2.

Katsaros, K. B., P. W. Vachon, P. G. Black, P. P. Dodge, and E. W. Uhlhorn, 2000: Wind fields from SAR: Could they improve our understanding of storm dynamics? *John Hopkins APL Tech. Digest*, **21**, 86–93.

Katsaros, K. B., P. W. Vachon, W. T. Liu, and P. G. Black, 2002: Microwave remote sensing of tropical cyclones from space. *J. Oceanography*, **58**, 137–151.

Keighton, S., D. K. Miller, D. Hotz, P. D. Moore, L. B. Perry, L. G. Lee, and D. T. Martin, 2016: Northwest Flow Snow Aspects of Hurricane Sandy. *Wea. Forecasting,* **31**, 173–195.

Kepert, J. D., 2006: Observed Boundary Layer Wind Structure and Balance in the Hurricane Core. Part I: Hurricane Georges. *J. Atmos. Sci.*, **63**, 2169-2193.

Kepert, J., 2012: Choosing a Boundary Layer Parameterization for Tropical Cyclone Modeling. *Mon. Wea. Rev.*, **140**, 1427–1445, doi: 10.1175/MWR-D-11-00217.1.

Kowaleski, A. and J. Evans, 2016: Regression Mixture Model Clustering of Multimodel Ensemble Forecasts of Hurricane Sandy: Partition Characteristics. *Mon. Wea. Rev.*, **144**, 3825–3846, doi: 10.1175/MWR-D-16-0099.1.

Lackmann, G., 2015: Hurricane Sandy before 1900 and after 2100. *Bull. Amer. Meteor. Soc.*, **96**, 547–560, doi: 10.1175/BAMS-D-14-00123.1.

Lin, N., J. A. Smith, G. Villarini, T. P. Marchok, and M. L Baeck, 2010: Modeling Extreme Rainfall, Winds, and Surge from Hurricane Isabel (2003). *Wea. Forecasting,* **25**, 1342-1361.

Lorsolo, S., J. L. Schroeder, P. Dodge, and F. Marks Jr., 2008: An Observational Study of Hurricane Boundary Layer Small-Scale Coherent Structures. *Mon. Wea. Rev.*, **136**, 2871–2893.

Lussier III, L. L., B. Rutherford, M. T. Montgomery, M. A. Boothe, T. J. Dunkerton, 2015: Examining the Roles of the Easterly Wave Critical Layer and Vorticity Accretion during the Tropical Cyclogenesis of Hurricane Sandy. *Mon. Wea. Rev.*, **143**, 1703–1722.

Magnusson, L., J.-R. Bidlot, S. Lang, A. Thorpe, N. Wedi, and M. Yamaguchi, 2014: Evaluation of medium-range forecasts for Hurricane Sandy. *Mon. Wea. Rev.*, **142**, 1962–1981.

Magnusson, L., A. Thorpe, M. Bonavita, S. Lang, T. McNally and N. Wedi, 2013: Evaluation of forecasts for hurricane Sandy. ECMWF Technical Memorandum No. 699, 28 pp.

Mass, C. and D. Ovens, 2010: WRF Model Physics: Problems, Solutions, and a New Paradigm for Progress. *WRF Users' Workshop*, Boulder, CO USA. June 21-25, 2010.

McNally, T., M. Bonavita, and J.-N. Thépaut, 2014: The Role of Satellite Data in the Forecasting of Hurricane Sandy. *Mon. Wea. Rev.*, **142**, 634–646.

Milrad, S.M., E. H. Atallah, and J. R. Gyakum, 2013: Precipitation Modulation by the Saint Lawrence River Valley in Association with Transitioning Tropical Cyclones. *Wea. Forecasting*, **28**, 331–352.

Mirocha, J., J. Lundquist, and B. Kosović, 2010: Implementation of a Nonlinear Subfilter Turbulence Stress Model for Large-Eddy Simulation in the Advanced Research WRF Model. *Mon. Wea. Rev.*, **138**, 4212–4228, doi: 10.1175/2010MWR3286.1.

Morrison, I., S. Businger, F. Marks, P. Dodge, and J. A. Businger, 2005: An Observational Case for the Prevalence of Roll Vortices in the Hurricane Boundary Layer. *J. Atmos. Sci.*, **62**, 2662-2673.

Munsell, E. B., and F. Zhang, 2014: Prediction and uncertainty of Hurricane Sandy (2012) explored through a real-time cloud-permitting ensemble analysis and forecast system assimilating airborne Doppler radar observations, *J. Adv. Model. Earth Syst.*, **6**, 38–58, doi:10.1002/2013MS000297.

Nakanishi, M., and H. Niino, 2006: An improved Mellor–Yamada level-3 model: Its numerical stability and application to a regional prediction of advection fog. *Bound.-Layer Meteor.*, **119**, 397–407.

Nakanishi, M. and H. Niino, 2012: Large-Eddy Simulation of Roll Vortices in a Hurricane Boundary Layer. *J. Atmos. Sci.*, **69**, 3558-3575.

Nolan, D. S., J. A. Zhang, and D. P. Stern, 2009: Evaluation of Planetary Boundary Layer Parameterizations in Tropical Cyclones by Comparison of In Situ Observations and High-Resolution Simulations of Hurricane Isabel (2003). Part I: Initialization, Maximum Winds, and the Outer-Core Boundary Layer. *Mon. Wea. Rev.*, **137**, 3651–3674.

Nolan, D., 2012: Overview of the PBL schemes in hurricane models, *HFIP Physics Workshop*, Clinton, MD, USA. 9-11 August 2011.

Obukhov, A. M., 1946: Turbulence in thermally non-homogeneous atmosphere. *Tr. Inst. Teor.Geofiz.Akad.Nauk SSSR*, **1**, 95–115.

Ramstrom, W., C. Lancaster, and R. Luo, 2016: Blackout Forecast Model for Hurricane Hazards – Wind and Surge. *32nd Conference on Hurricanes and Tropical Meteorology*, 17 – 22 April 2016, San Juan, PR.

Raveh-Rubin, S. and H. Wernli, 2015: Climatology of dry air intrusions and their relation to strong surface winds in extratropical cyclones. Fifth Workshop on European Storms, Bern, Switzerland. August 31, 2015.

Roux, G., Y. Liu, L. Delle Monache, R.-S. Sheu, and T. T. Warner, 2009: Verification of high resolution WRFRTFDDA surface forecasts over mountains and plains. Preprints, 10th WRF Users Workshop, Boulder, CO, NCAR.

Santos-Alamillos, F. J., D. Pozo-Va ´Zquez, J. A. Ruiz-Arias, V. Lara-Fanego, and J. Tovar-Pescador, 2013: Analysis of WRF Model Wind Estimate Sensitivity to Physics Parameterization Choice and Terrain Representation in Andalusia (Southern Spain). *J. Appl. Meteor. Climatol.*, **52**, 1592-1609.

Schiavone, J. A., P. Johnsen, D. A. Robinson, M. Gerbush and A. Norton, 2016: Mesoscale comparison of simulated and observed winds during Sandy's landfall on New Jersey. *WRF Users' Workshop*, Boulder, CO USA. June 28, 2016.

Shapiro, M. A., T. J. Galarneau Jr., J. Vigh, A. Norton, and C. S. Velden, 2013: The Life Cycle of Hurricane Sandy: Observations; Simulations; Operational Forecasts; Socioeconomic Impacts. 15th Conference on Mesoscale Processes, Portland, OR, USA, August 06 - 09, 2013.

Shin, H. H., and J. Dudhia, 2015: Evaluation of PBL Parameterizations in WRF at Sub-Kilometer Resolution: Turbulence Statistics in the Convective Boundary Layer. *Geophysical Res. Abstracts*, **17**, EGU2015-4172.

Shin, H. H and S.-Y. Hong, 2011: Intercomparison of Planetary Boundary-Layer Parametrizations in the WRF Model for a Single Day from CASES-99. *Boundary-Layer Meteorol.*, **139**, 261–281. doi: 10.1007/s10546-010-9583-z

Shin, H. and S. Hong, 2015: Representation of the Subgrid-Scale Turbulent Transport in Convective Boundary Layers at Gray-Zone Resolutions. *Mon. Wea. Rev.*, **143**, 250–271, doi: 10.1175/MWR-D-14-00116.1.

Shin, J. H., and D.-L. Zhang, 2017: The Impact of Moist Frontogenesis and Tropopause Undulation on the Intensity, Size, and Structural Changes of Hurricane Sandy (2012). *J. Atmos. Sci.*, **74**, 893-913.

Simpson, R. H., 1974: The Hurricane Disaster Potential Scale. *Weatherwise*, **27**, 169-186.

Skamarock, W. C., 2004: Evaluating mesoscale NWP models using kinetic energy spectra. *Mon. Wea. Rev.*, **132**, 3019–3032.

Sobel, A., 2014: *Storm Surge: Hurricane Sandy, Our Changing Climate, and Extreme Weather of the Past and Future.* Harper Wave, 336 pp.

Stull, R. B., 1988: *An Introduction to Boundary Layer Meteorology*. Kluwer Academic, 666 pp.

Sukoriansky, S., B. Galperin, V. Perov. 2006: A quasi-normal scale elimination model of turbulence and its application to stably stratified flows. *Nonlinear Processes in Geophysics*, **13**, 9-22.

Talbot, C., E. Bou-Zeid, and J. Smith, 2012: Nested Mesoscale Large-Eddy Simulations with WRF: Performance in Real Test Cases. *J. Hydrometeor.*, **13**, 1421–1441, doi: 10.1175/JHM-D-11-048.1.

Tewari, M., F. Chen, W. Wang, J. Dudhia, M. A. LeMone, K. Mitchell, M. Ek, G. Gayno, J. Wegiel, and R. H. Cuenca , 2004: Implementation and verification of Unified Noah land surface model in the WRF model, *84th AMS Conference*, Seattle, Wash., 11–15 January 2004.

Tongue, J., 2014: Hurricane Sandy – Boundary Layer Structure Effects on Winds and Storm Surge. Fifth Tri-State Weather Conference, Danbury, CT USA. October 12, 2014.

Torn, R. D., J. S Whitaker, P. Pegion, T. M. Hamill, and G. J. Hakim, 2015: Diagnosis of the Source of GFS Medium-Range Track Errors in Hurricane Sandy (2012). *Mon. Wea. Rev.*, **143**, 132–152.

Van Den Broeke, M. S., 2013: Polarimetric Radar Observations of Biological Scatterers in Hurricanes Irene (2011) and Sandy (2012). *J. Atmos. Oceanic* Technol., **30**, 2754–2767.

Veiga, J. A. P., and Queiroz, M. R., 2015: Impact of the Waves on the Sea Surface Roughness under Uniform Wind Conditions: Idealized Cases for Uniform Winds (Part I). *Atmos. Climate Sci.*, **5**, 317-325.

Vigh, J. L., P. Johnsen, M. Straka, T. Galarneau, E. Uhlhorn, A. Norton, N. M. Dorst, F. Marks, Jr., and M. Shapiro, 2013: Evaluation of the Simulated Structure of Hurricane Sandy Using Synthetic Flight Paths. *16th Cyclone Workshop,* Sainte-Adèle, Quebec, Canada, 22-27 September 2013.

Wang, H. V., J. D. Loftis, Z. Liu, D. Forrest, and J. Zhang, 2014: The Storm Surge and Sub-Grid Inundation Modeling in New York City during Hurricane Sandy. *J. Mar. Sci. Eng*., **2**, 226-246, doi:10.3390/jmse2010226.

Wang, W., C. Bruyère, M. Duda, J. Dudhia, D. Gill, H.-C. Lin, J. Michalakes, S. Rizvi, and X. Zhang., 2012: Land Use and Soil Categories in the Static Data. *WRF ARW Version 3 Modeling System User's Guide*, NCAR Mesoscale and Microscale Meteorology Division.

Worsnop, R., 2016: Using Large-eddy Simulations to Examine the Variability of Wind Speed and Direction in the Hurricane Boundary Layer. 22nd Symposium on Boundary Layers and Turbulence. June 20, 2016.

Wurman, J. and J. Winslow, 1998: Intense Sub-Kilometer-Scale Boundary Layer Rolls Observed in Hurricane Fran. *Science*, *280*, 555-557, doi: 10.1126/science.280.5363.555.

Wyngaard, J., 2004: Toward Numerical Modeling in the "Terra Incognita*". J. Atmos. Sci*., **61**, 1816–1826, doi: 10.1175/1520-0469(2004)061<1816:TNMITT>2.0.CO;2.

Xiang, B., S.-J. Lin, M. Zhao, S. Zhang, G. Vecchi, T. Li, X. Jiang, L. Harris, J.-H. Chen, 2015: Beyond Weather Time-Scale Prediction for Hurricane Sandy and Super Typhoon Haiyan in a Global Climate Model. *Mon. Wea. Rev.*, **143**, 524–535.

Xie, B. and J. C. H. Fung, 2014: A comparison of momentum mixing models for the planetary boundary layer. *J. Geophysical. Res.: Atmos*., **119**, 2079-2091.

Yang, M.-J., D.-L. Zhang, and H.-L. Huang, 2008: A Modeling Study of Typhoon Nari (2001) at Landfall. Part I: Topographic Effects. *J. Atmos. Sci*., **65**, 3095–3115.

Yang, J., M. Astitha, E. N. Anagnostou, and B. M. Hartman, 2017: Using a Bayesian Regression Approach on Dual-Model Windstorm Simulations to Improve Wind Speed Prediction. *J. Appl. Meteor. Climate*, **56**, 1155-1174.

Zhang, F., 2016: Examining the Impact of Different Vertical Mixing Strengths on Hurricanes Evolution over Land. 22nd Symposium on Boundary Layers and Turbulence. June 22, 2016.

Zhang, J. A., K. B., Katsaros, P. G. Black, S. Lehner, J. R. French, and W. M. Drennan, 2008: Effects of roll vortices on turbulent fluxes in the hurricane boundary layer. *Bound.-Layer Meteor.*, **128**, 173–189.

Zhang, D. and R. Anthes, 1982: A High-Resolution Model of the Planetary Boundary Layer—Sensitivity Tests and Comparisons with SESAME-79 Data. *J. Appl. Meteor*., **21**, 1594–1609, doi: 10.1175/1520-0450(1982)021<1594:AHRMOT>2.0.CO;2.

Zhang, J. A., and E. W. Uhlhorn, 2012: Hurricane Sea Surface Inflow Angle and an Observation-Based Parametric Model. *Mon. Wea. Rev.*, **140**, 3587–3605.

Zhang, F., Z. Pu , and C. Wang, 2017: Effects of boundary layer vertical mixing on the evolution of hurricanes over land. *Mon. Wea. Rev*., **145**, 2343-2361.

Zhang, F. and Z. Pu , 2017: Effects of vertical diffusion of surface heat and moisture fluxes on the evolution of landfalling hurricanes. *J. Atmos. Sci*., **74**, 1879-1905.

Zhu, P., 2008: Simulation and parameterization of the turbulent transport in the hurricane boundary layer by large eddies. *J. Geophys. Res*., **113**, D17104.

Zhu, T., S. A. Boukabara, and K. Garrett, 2017: Comparing Impacts of Satellite Data Assimilation and Lateral Boundary Conditions on Regional Model Forecasting: A Case Study of Hurricane Sandy (2012). *Wea. Forecasting*, **32**, 595–608.

TABLE 1. Data sources, where all but the last line shows observation data. For the WRF simulation data in the last line, the "Number of Sites" is the number of horizontal grid points and the "Wind Sensor Elevation" is the depth of the model domain studied in detail.

Data Source	Number of Sites	Wind Sensor Elevation (m)	Observation Interval	Geographical Domain
NJWxNet	46	2.8 – 12.1	5 minutes	New Jersey
DEOS	46	3	5 minutes	Delaware, Southeastern PA
ASOS	22	10	5 minutes	New Jersey, Delaware, Eastern PA, Southern NY
NDBC	12	3.5 – 23.0	5 to 60 minutes	Delaware Bay, Long Island Sound, Atlantic Bight
Rawinsonde	3	10 – 2,600	6 hours	Upton, NY (OKX), Wallops Island, VA (WAL), Sterling, VA (IAD)
WSR-88D	1	300 – 15,000	6 minutes	Fort Dix, NJ (DIX)
WRF	10^6	10 – 3,500	30 minutes	71.5 – 77.5°W, 37.3 – 41.9°N

TABLE 2. WRF simulation specifications.

Attribute	Description
Simulation system	Advanced Research WRF version 3.3.1
Hardware system	Cray XE6 "Blue Waters" at NCSA
Execution time	58 hours of wall clock using 140,000 cores
Grid specification	500 meter spacing, 5320x5000 horizontal grid points, 150 layers
Initialization and boundary conditions	NOAA/NCEP GFS global model output initialized at 1200 UTC 26 October 2012 with boundary conditions updated every 6 hours
PBL parameterization	Yonsei University (YSU)
Surface layer model	MM5 Monin-Obukhov similarity theory
Land surface model	Noah
Radiation model	RRTM/Dudhia long and shortwave radiation schemes
Cumulus model	Explicit
Microphysics	WSM6 6-class microphysics with graupel
Core physics	Full non-hydrostatic forecast with full moist physics
Integration step	1.25 second with cold start
Simulation period	96 hours, 1200 UTC 26 October 2012 to 1200 UTC 30 October 2012
Archived output	30 minute interval, 193 files, 224 Gigabytes each, total of 43.2 Terabytes

TABLE 3. Spatiotemporally averaged wind speeds for the 4 hour period bracketing landfall time of 0000 UTC October 30 for the 10 regions described in section 4a, where (a) lists observations, (b) lists WRF simulation results at observation locations and (c) lists ratios of WRF simulated average wind speeds to observed average wind speeds. Bold entries in (a) and (b) identify maximum values among regional sets. Bold entries in (c) identify ratios less than one, i.e. for which WRF under-predicted wind speeds.

(a) Observed spatiotemporally averaged wind speeds.

Land Region	Interior	Coastal	Water Region	Coastal	Open
North of Track	8.5	**15.0**	Long Island Sound	18.4	–
Along Track	7.9	7.5	Ocean	**28.3**	12.0
South of Track	10.4	14.2	Delaware Bay	15.4	–

(b) WRF simulation spatiotemporally averaged wind speeds at observation locations.

Land Region	Interior	Coastal	Water Region	Coastal	Open
North of Track	12.1	14.3	Long Island Sound	17.1	–
Along Track	12.8	15.7	Ocean	**26.0**	13.3
South of Track	13.9	**18.3**	Delaware Bay	19.7	–

(c) Ratios of WRF simulation average wind speeds to observed average wind speeds.

Land Region	Interior	Coastal	Water Region	Coastal	Open
North of Track	1.43	**0.96**	Long Island Sound	**0.93**	–
Along Track	1.61	2.09	Ocean	**0.92**	1.10
South of Track	1.34	1.29	Delaware Bay	1.28	–
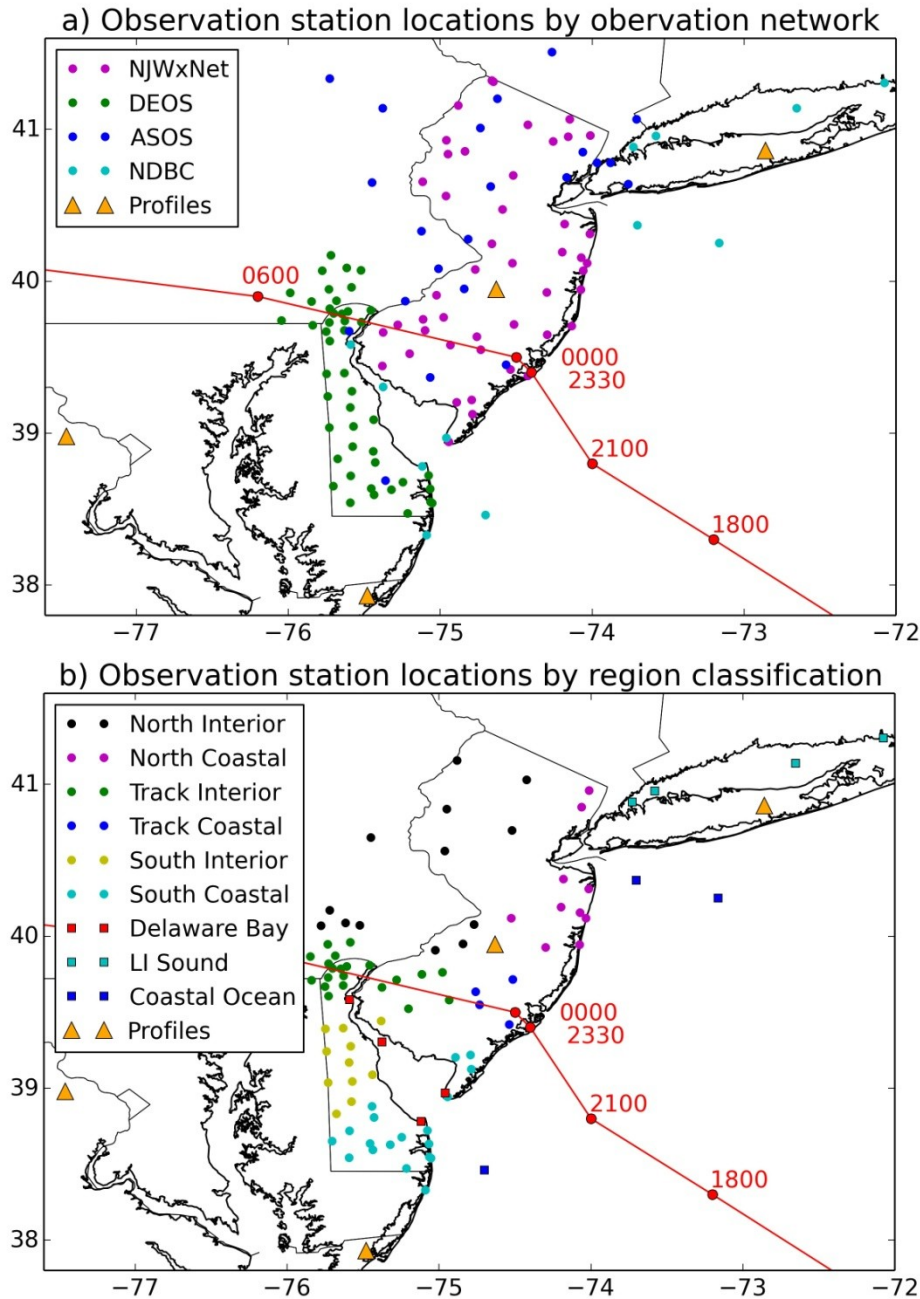
FIG. 1. (a) Locations of observation stations that provided usable wind speed data, with observation networks identified by colors shown in the legend. Orange triangle in central New Jersey is Fort Dix WSR-88D site for which velocity azimuth display (VAD) wind profiles are available. Remaining 3 triangles are rawinsonde sites and red line is the NHC best track for Hurricane Sandy from Table 1 of Blake et al. (2013), where displayed track begins at 1800 UTC 29 October 2012. (b) Regional classification of surface observation stations used in Fig. 9 as described in section 4a and in Table 3 as described in section 4d.
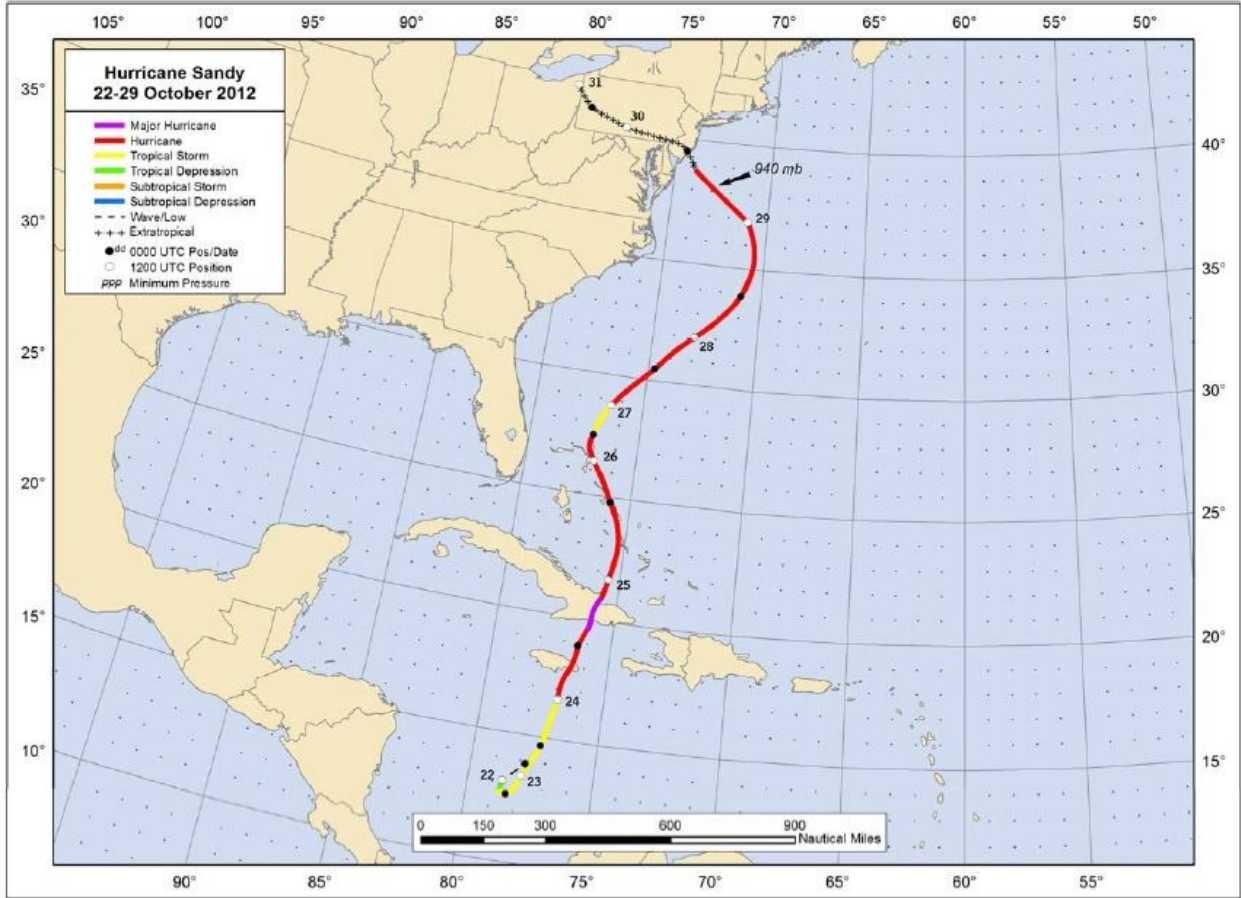
FIG. 2. NHC best track for Hurricane Sandy from Fig. 1 of Blake et al. (2013).
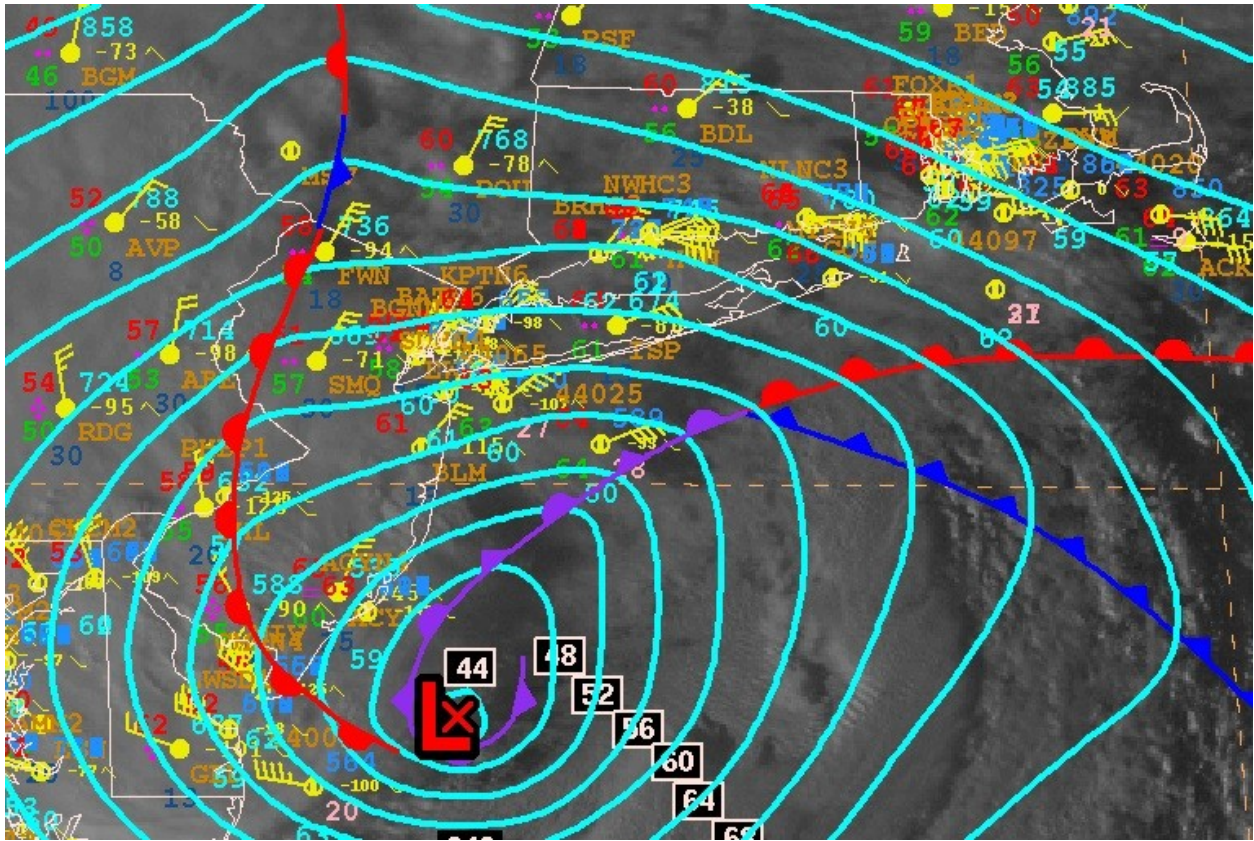
FIG. 3. NHC analysis of post-tropical cyclone Sandy from Fig. 23 of Blake et al. (2013) at 2100 UTC 29 October 2012, the time at which NHC declared the cyclone to have transitioned to extratropical.
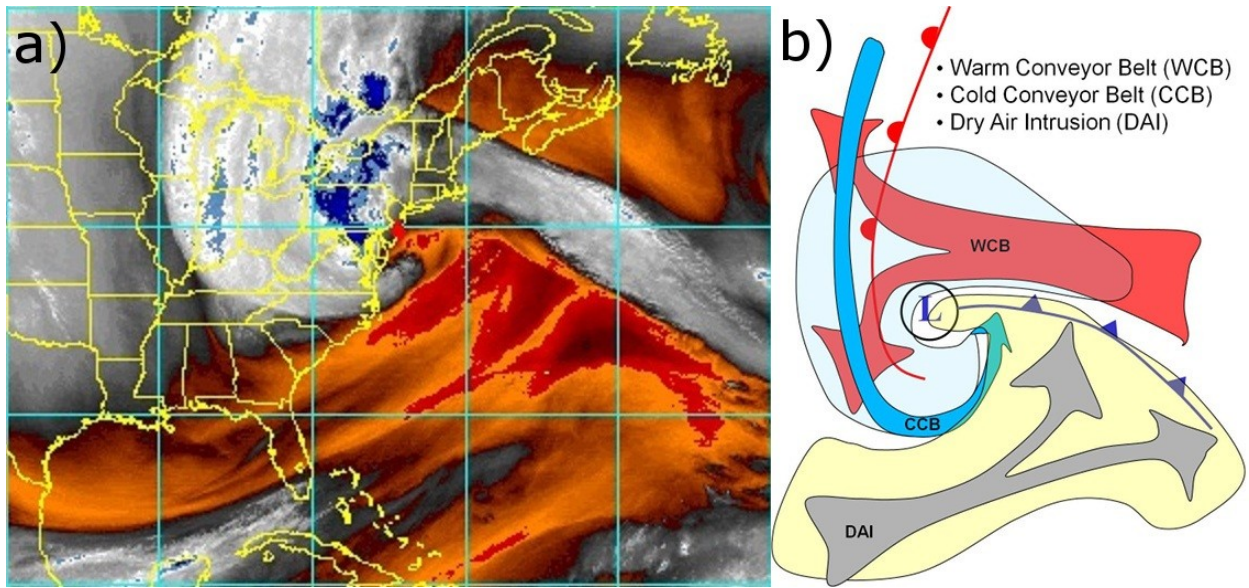
FIG. 4. (a) GOES water vapor image of post-tropical cyclone Sandy at 2345 UTC 29 October 2012. (b) Illustration of classic airstreams associated with an extratropical cyclone, adapted from Raven-Rubin and Wernli (2015). Pink arrow on illustration is warm conveyor belt (WCB) which corresponds to grey airstream on GOES image, blue arrow on illustration is cold conveyor belt (CCB) which corresponds to white airstream on GOES image, and grey arrow on illustration is descending dry air intrusion (DAI) which corresponds to orange airstream on GOES image.
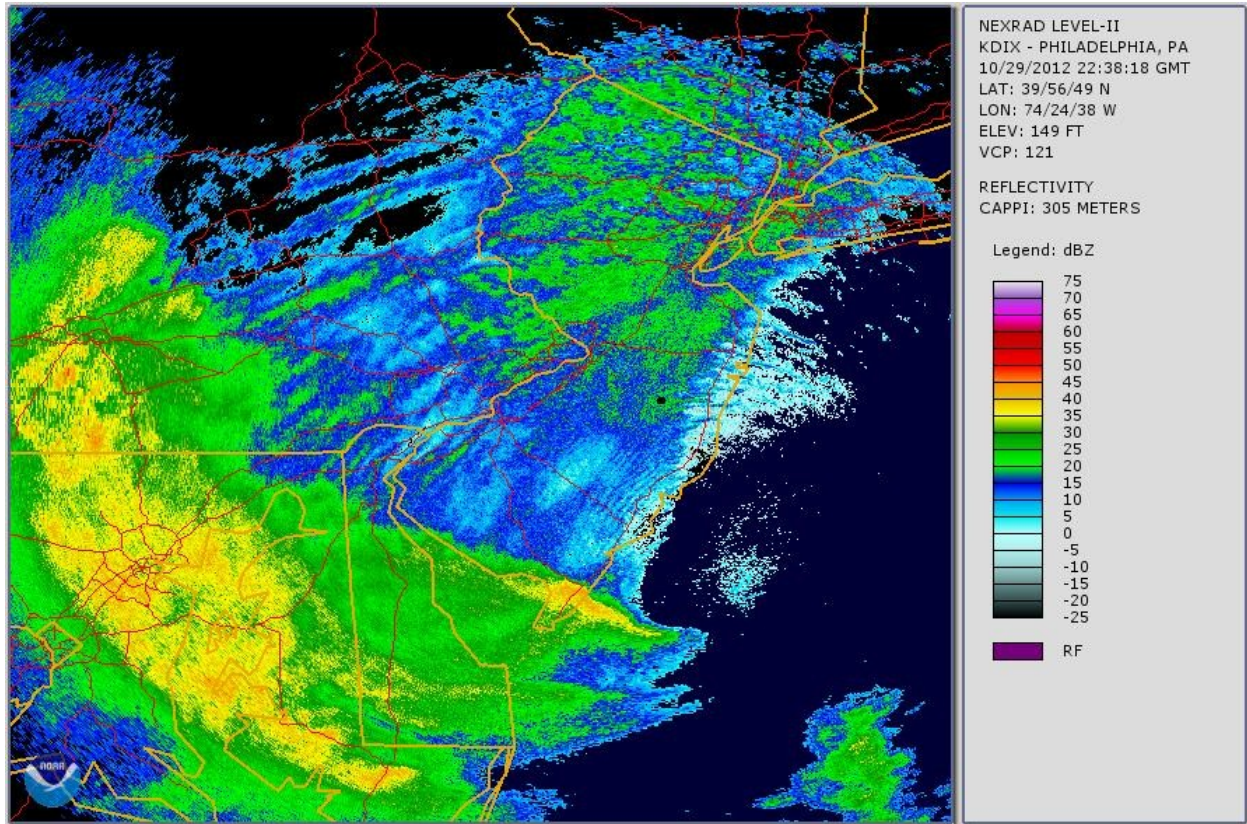
FIG. 5. Fort Dix, NJ WSR-88D reflectivity at 305 meter elevation at 2238 UTC 29 October 2012. Yellow and green arc in southwest quadrant is deep convection southwest of surface convergence zone and warm front, as identified on Fig. 3. Blue and green swath extending northeastward from deep convection is shallow precipitation within warm conveyor belt. Light blue arc along northern New Jersey coast is leading edge of descending dry air intrusion near surface. Linear features oriented southwest to northeast within blue and green shallow precipitation swath are thought to be associated with roll vortices, also known as large eddy circulations, in the PBL.
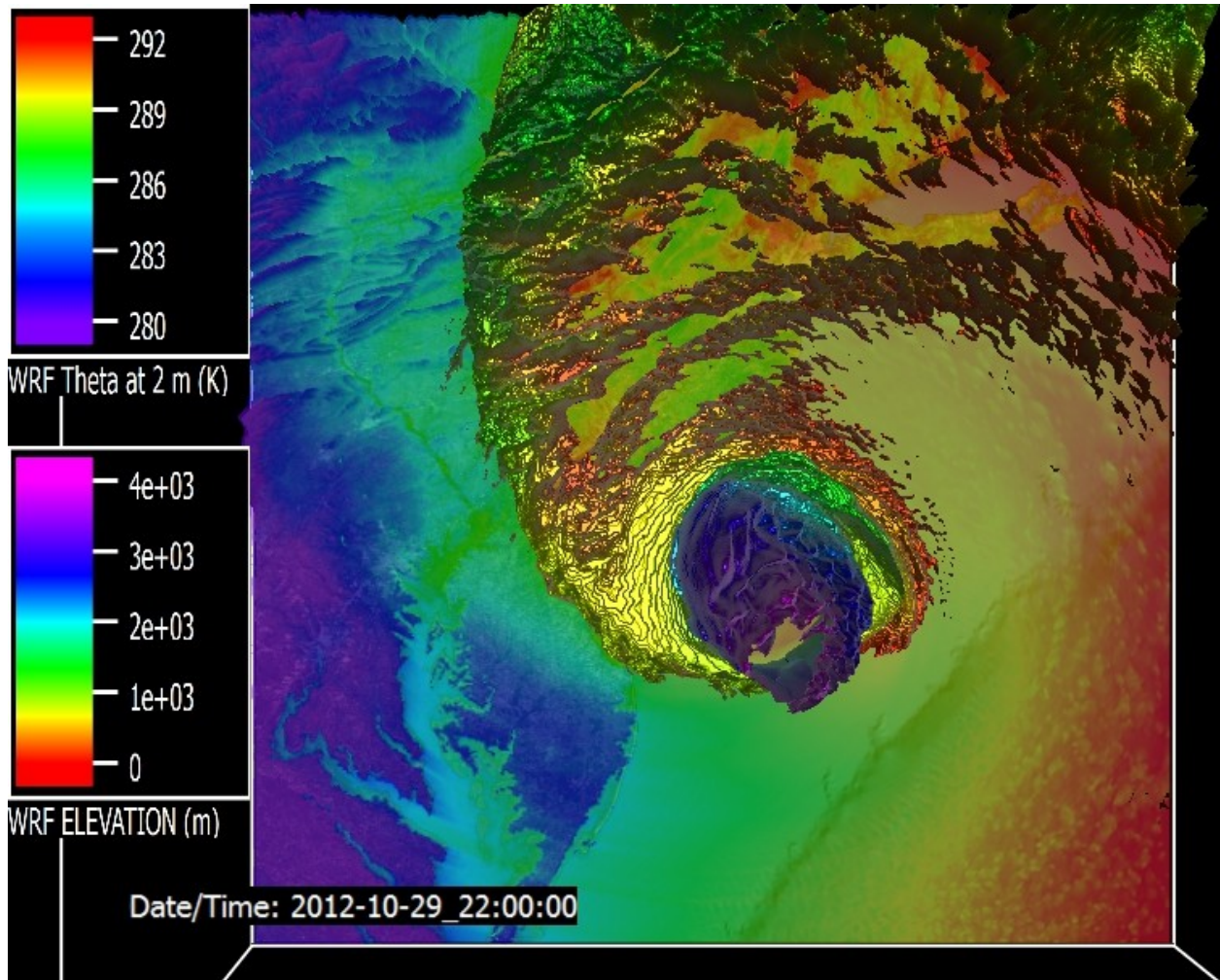
FIG. 6. WRF simulation results at 2200 UTC 29 October 2012 showing 2 meter temperature as an earth-based color image and the top surface of a volume that encloses highest values of water vapor mixing ratio. Elevation of the water vapor surface is denoted by color, where red is low and violet is high elevation. Simulation evidence that moist air of the warm conveyor belt is being etched away from above by the descending dry air intrusion north of the storm center are the streaks of the top surface of highest water vapor concentration, which slope downward from the warm front (green surface) toward the east (red surface) and further eastward disappear completely.
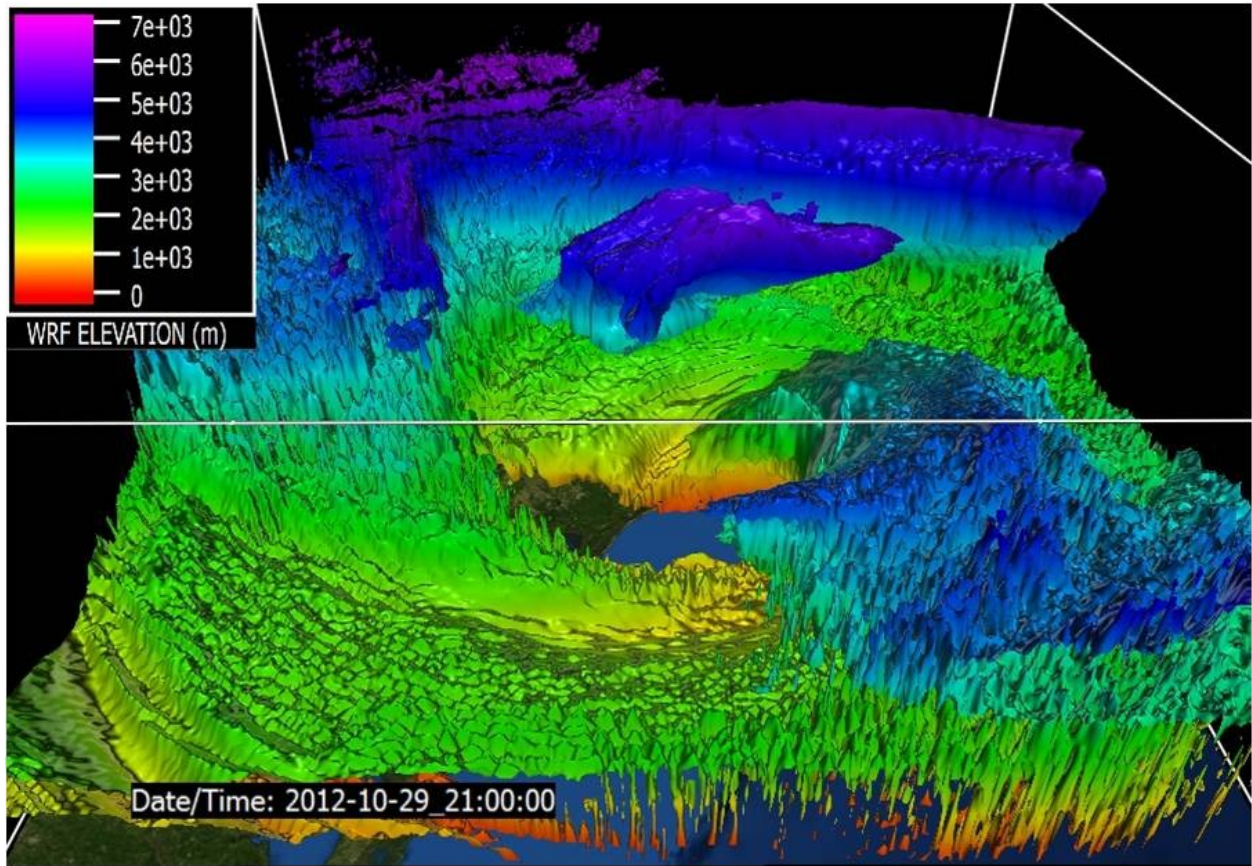
FIG. 7. WRF simulation results at 2100 UTC 29 October 2012 showing outer surface enclosing simulated wind speeds that exceed 34 m s^{-1}. Elevation of surface is shaded by color, with red low and violet high elevation. The blue arc along the northern and western edges of the domain appears to be the cold conveyor belt, the green and yellow swath north of the storm center appears to be the warm conveyor belt, and the blue arc in the southeast quadrant of the domain appears to be the descending dry air intrusion.
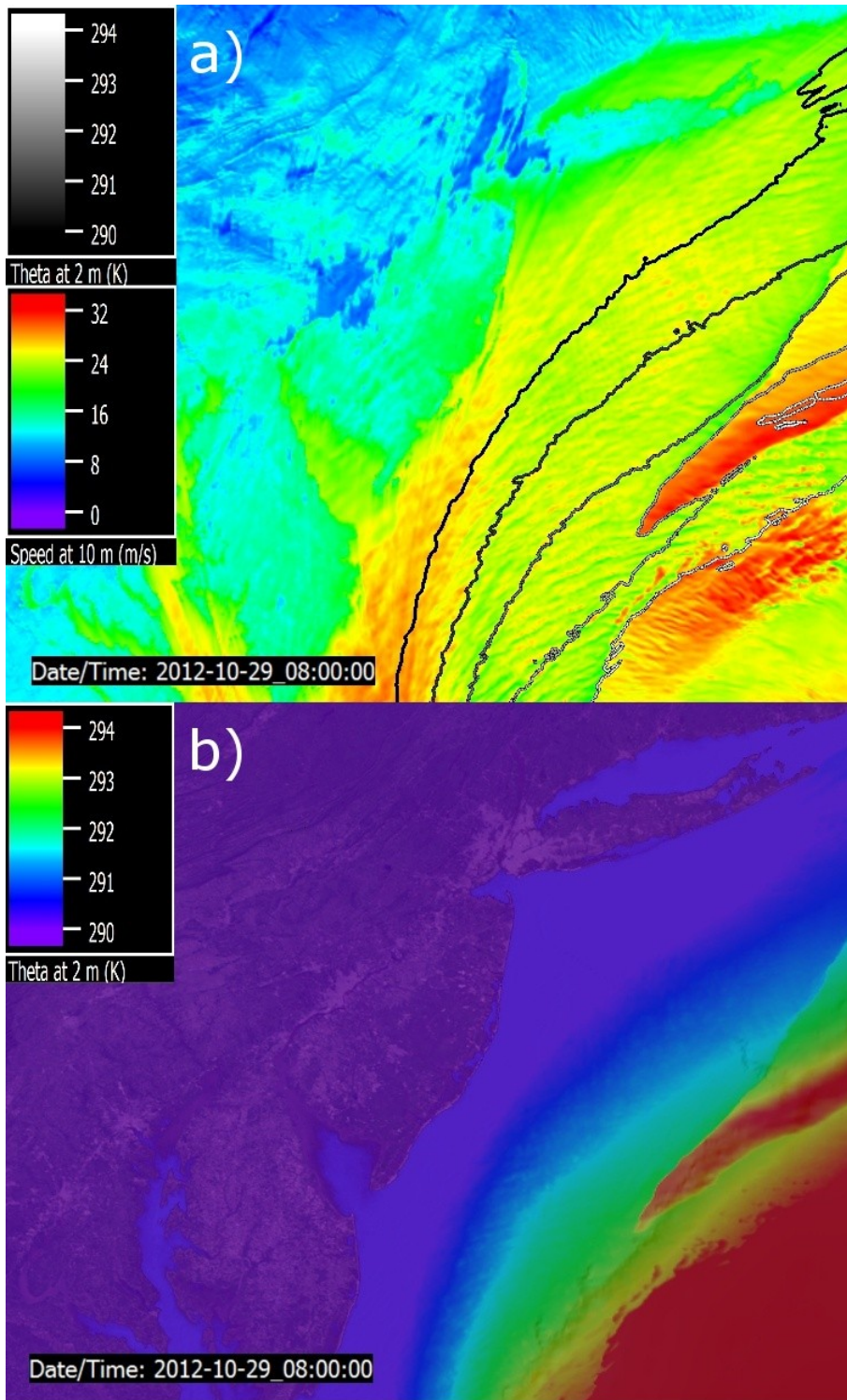
FIG. 8. WRF simulation results at 0800 UTC 29 October 2012 showing surface warm wind speed dart, protruding into the frame from its eastern edge. (a) shows 10 meter wind speed as color shading and 2 meter temperature as contours. (b) shows 2 meter temperature as color shading that emphasizes the temperature range in and around the dart feature.
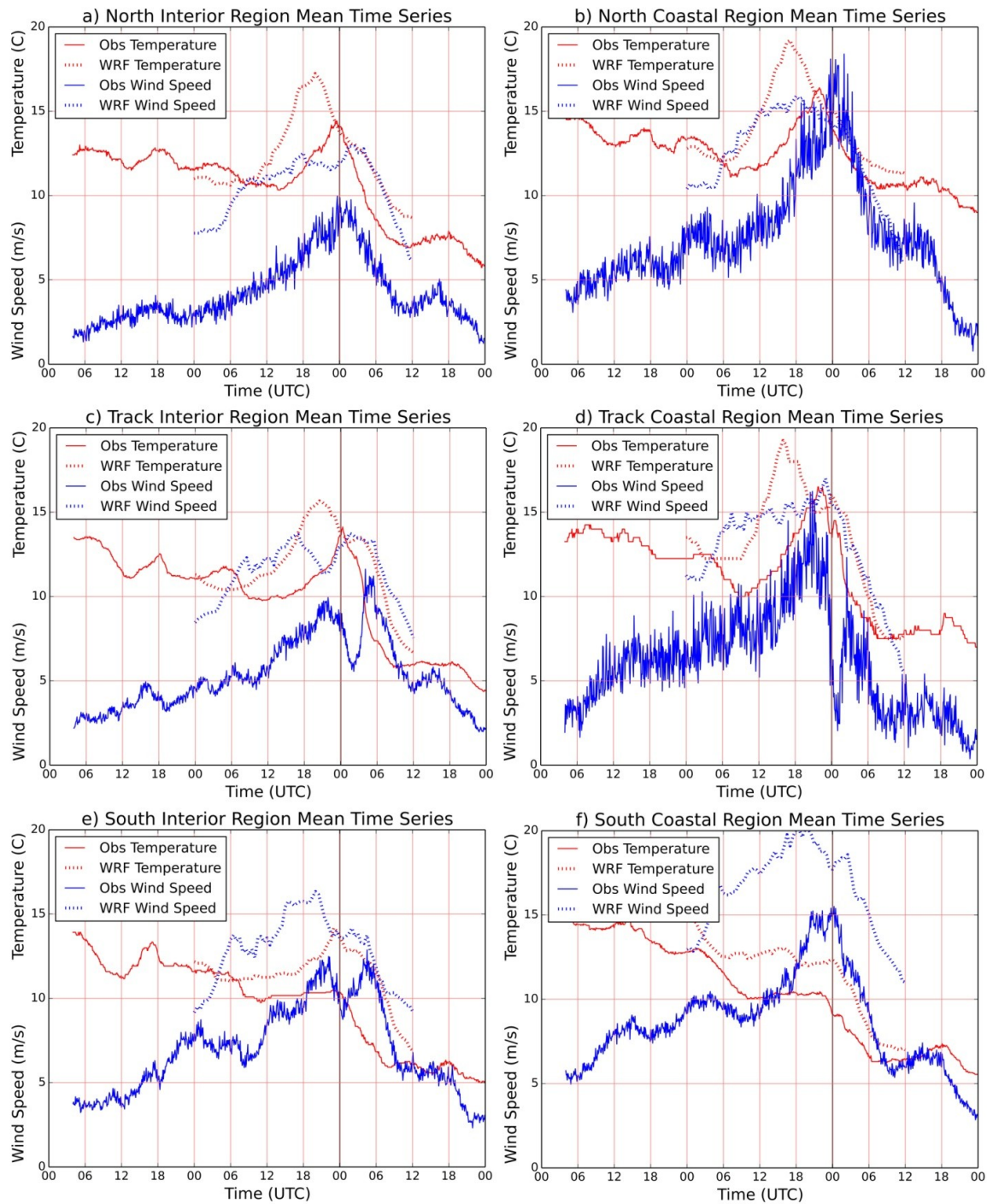
FIG. 9. Regionally averaged time series of surface wind speed (blue) and temperature (red), with observations as solid and WRF simulation results as broken lines. Six frames are arranged geographically, with those on the left (a, c, e) being inland, those on the right (b, d, f) being coastal, those at the top (a, b) being north of the storm track, those at the bottom (e, f) being south of the track, and those in the middle (c, d) being along the track. The heavier vertical line at 0000 UTC 30 October 2012 denotes nominal landfall time.

38
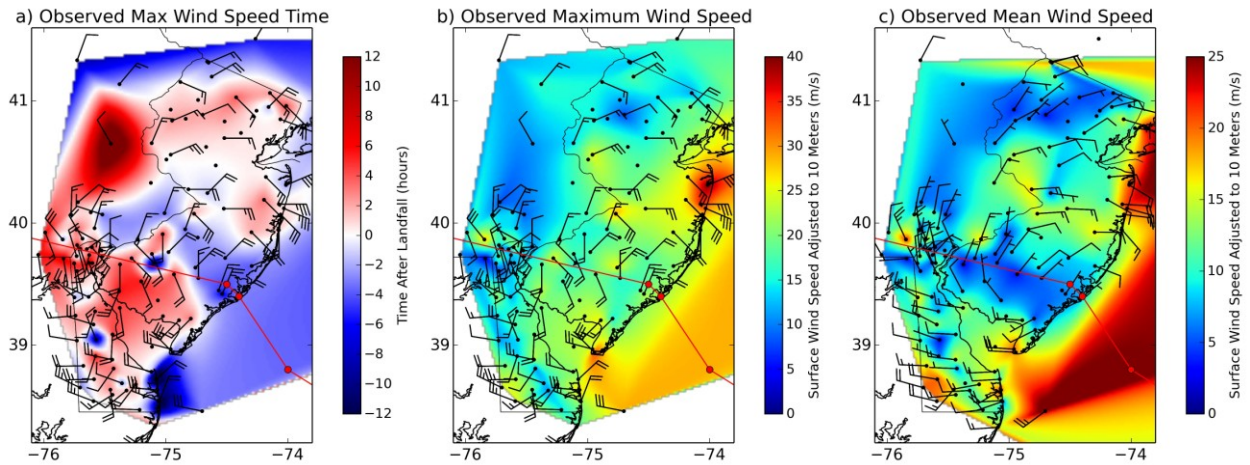
FIG. 10. Observed surface winds. (a) Time of maximum wind speed at stations, relative to nominal landfall time of 0000 UTC 30 October 2012. Time is interpolated to a color image, with blue before and red after landfall. Barbs depict maximum wind speed and associated direction at stations. (b) Maximum wind speed at stations interpolated to a color image with barbs depicting maximum wind speed and associated direction at stations. (c) 4 hour mean wind speed symmetrically bracketing nominal landfall time of 0000 UTC 30 October 2012, with mean wind speed at stations interpolated to a color image and barbs depicting mean wind speed and direction at stations.
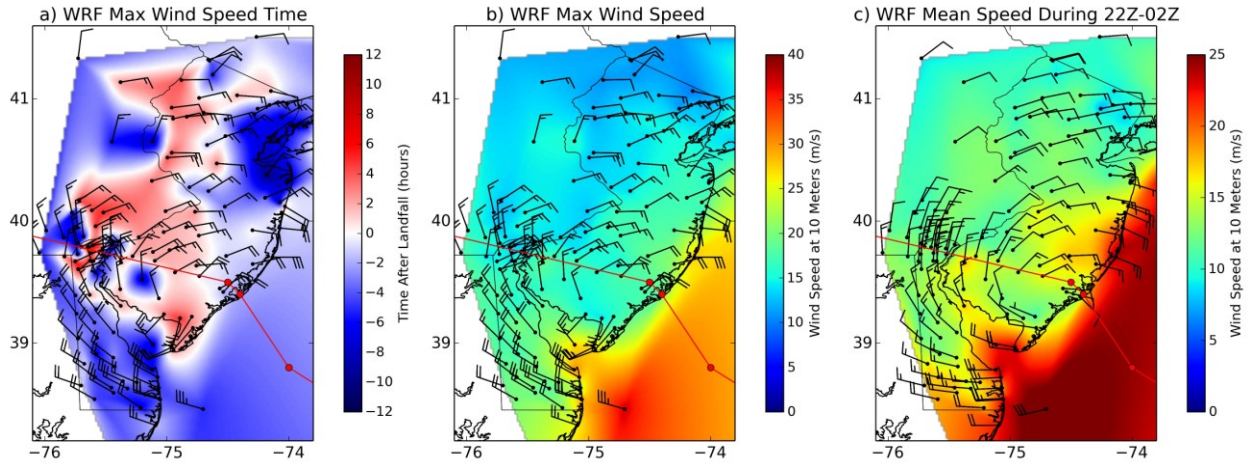
FIG. 11. WRF simulated surface winds interpolated to surface observation station locations. (a) Time of maximum wind speed at stations, relative to nominal landfall time of 0000 UTC 30 October 2012. Time is interpolated to a color image, with blue before and red after landfall. Barbs depict maximum wind speed and associated direction at stations. (b) Maximum wind speed at stations interpolated to a color image with barbs depicting maximum wind speed and associated direction at stations. (c) 4 hour mean wind speed symmetrically bracketing nominal landfall time of 0000 UTC 30 October 2012, with mean wind speed at stations interpolated to a color image and barbs depicting mean wind speed and direction at stations.
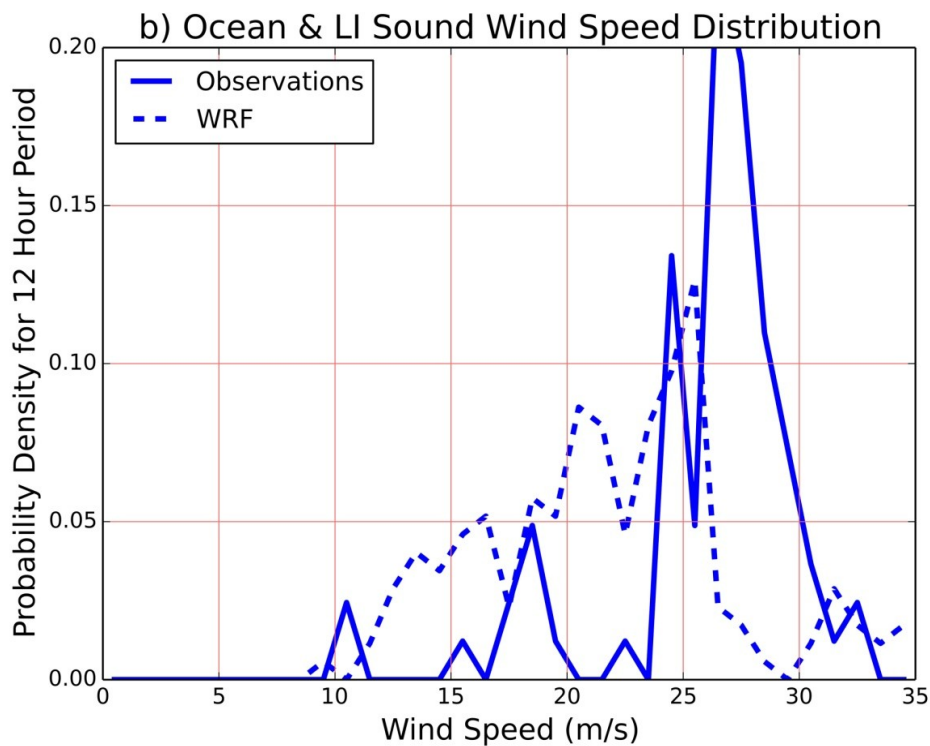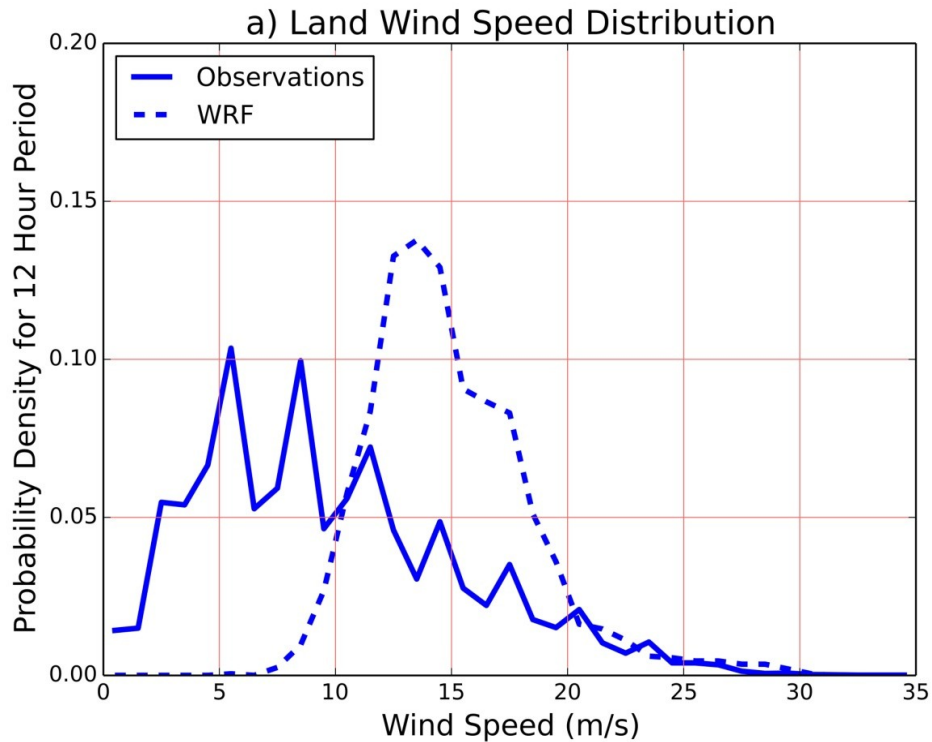
FIG. 12. Comparisons of observed and WRF simulated wind speed distributions during 12 hour period of 1600 through 0400 UTC 30 October 2012 for (a) land and (b) ocean and Long Island Sound stations. There are 79 land and 7 over-water stations. Observations are solid and WRF simulation results are broken lines.
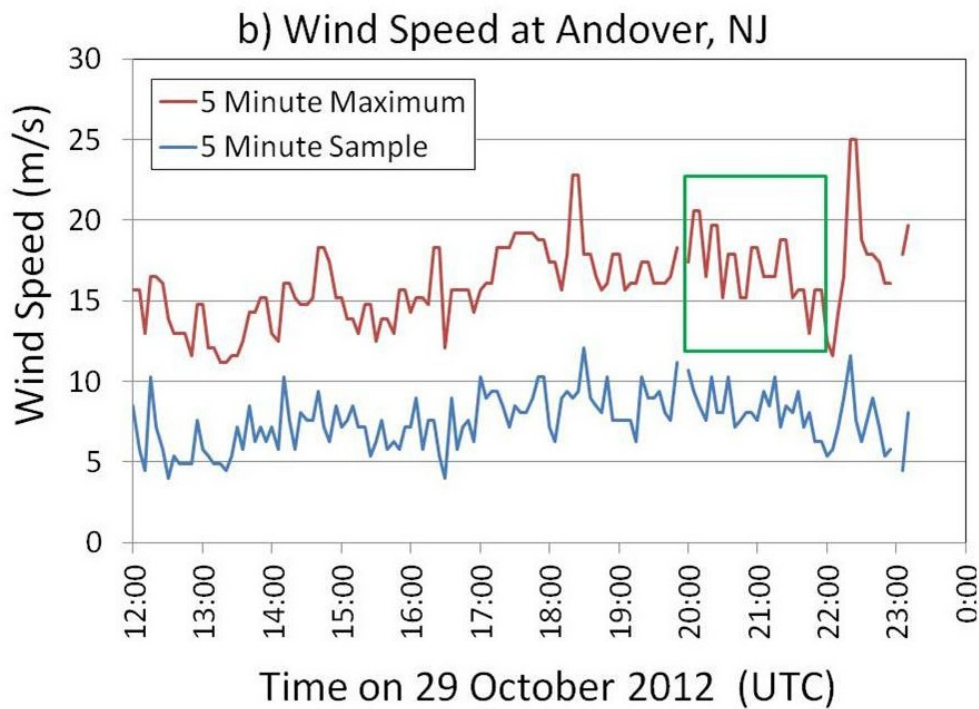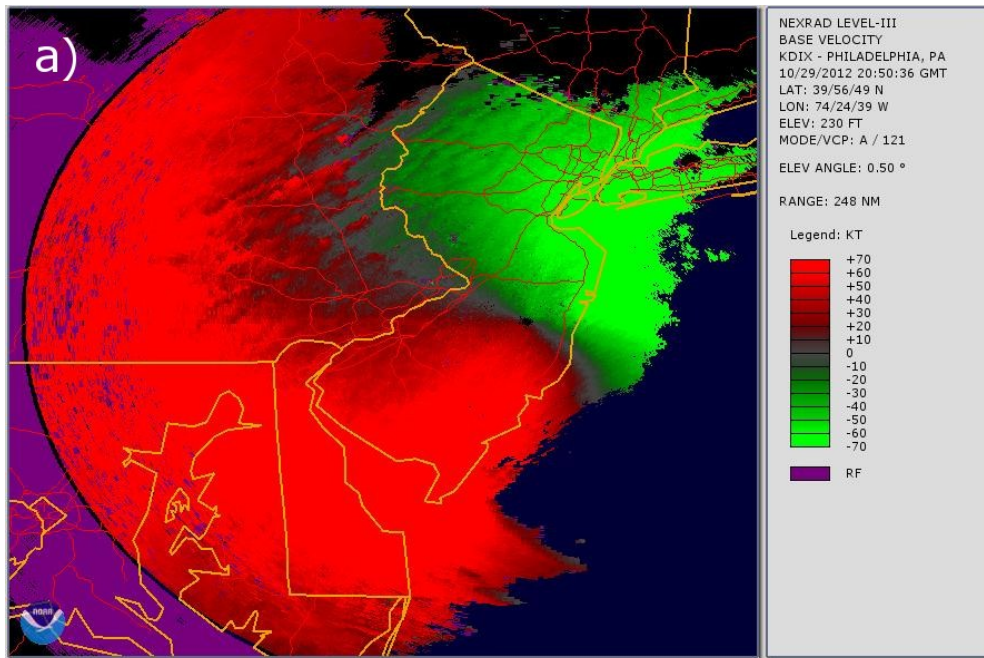
FIG. 13. Possible large eddy circulation signatures in observations of (a) WSR-88D radial velocity image at 2050 UTC 29 October 2012 and (b) wind speed time series at Andover, NJ during 1200 through 0000 UTC 30 October 2012. In (a) green is wind toward and red is wind away from the radar site. In (b), red plots ASOS observations of maximum wind speed at 5 minute intervals and blue plots ASOS observations of mean 2 minute wind speed. The green box identifies possible periodicity in maximum wind speed of about 15 minutes which agrees with that deduced from radar imagery.
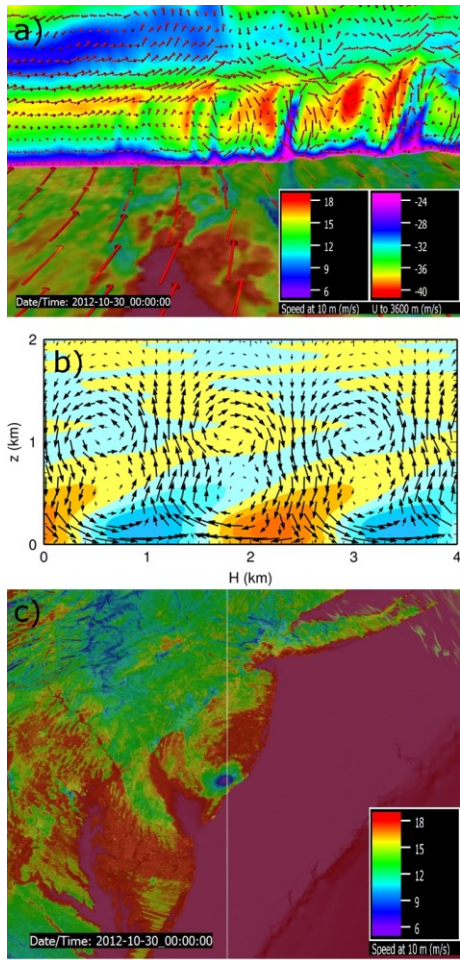
FIG. 14. (a) WRF simulation of wind field exhibiting possible large eddy circulation, or roll vortex, signatures, viewed from the east. Top half of frame is a north-south vertical cross section of wind field through center of simulated storm at 0000 UTC 30 Oct 2012 with (c) depicting its baseline as a vertical white line and its approximately 50x90 km horizontal domain as a black rectangle. Color shading on cross section represents west-to-east (U) component of wind, i.e. tangential wind vector relative to storm center. Red is high and violet is low velocity away from the viewpoint. Red arrows on cross section depict south-to-north (V) and vertical (W) components of wind, i.e. radial wind vector relative to storm center. Bottom half of frame is a horizontal ground level image that represents 10 meter wind speed, with large red arrows representing 10 meter wind vector. (b) Large eddy simulation of hurricane boundary layer large eddy circulation (roll vortex) wind field by Nakanishi and Niino (2012), showing vertical cross section of along-roll velocity fluctuation (difference from mean velocity) as color shading and cross-roll velocity fluctuation as vectors. Orange is away from and blue is toward viewer. (c) WRF simulated 10 meter wind speed at same time as (a) and using same color scale. North-south white line is baseline for cross section in (a), with arrow depicting viewpoint of (a) and black rectangle depicting horizontal domain of (a), which is about 50x90 km.
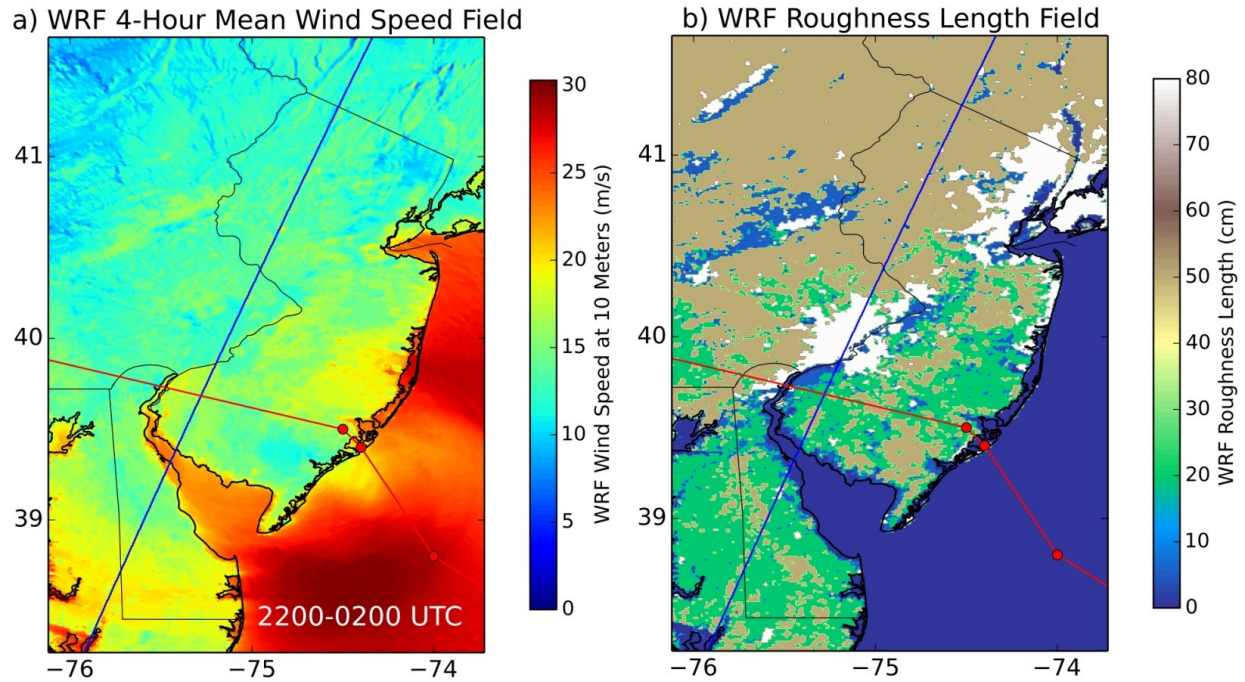
FIG. 15. WRF surface fields, with blue line locating baseline for horizontal profile shown in <mark>Fig. 16</mark> and red line locating post-tropical cyclone Sandy track. (a) shows wind speed at 10 meters averaged over 4 hours symmetrically bracketing nominal landfall time. (b) shows roughness length, z_0, which is used as model input for WRF parameterization computation of 10 meter wind speed.
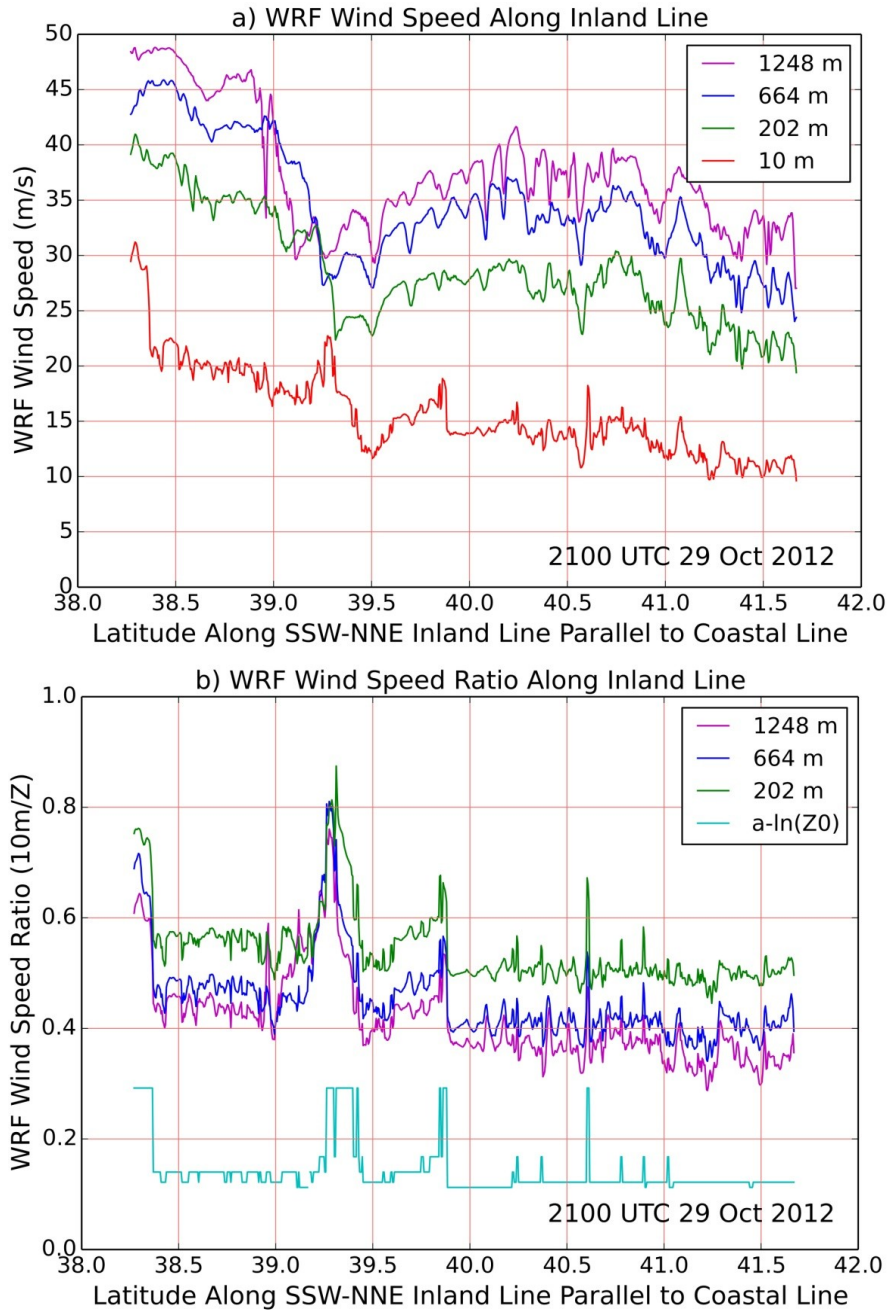
FIG. 16. Horizontal profiles of WRF simulated wind speed at 2100 UTC 29 October 2012 along baseline shown as blue line in Fig. 15. (a) Wind speed at 4 model levels, where upper 3 elevations shown in legend are approximate middle elevations of model layers and lowest elevation is 10 meters above surface of the earth. (b) Ratio of surface wind speed at 10 meters to that at 3 higher elevations. Also shown as cyan line is the quantity $a - \ln(z_0)$ which is an arbitrarily-scaled and inverted representation of z_0, with minimum z_0 values at water bodies exhibited as upward "plateaus" and spikes on plot. This scaling emphasizes the correlation of local maxima in wind speed predictions with minimum z_0 values of water bodies.

Supplemental Material

S-1. Data dissection and visualization

Because of the large volume of high-resolution mesoscale simulation data that was available for this study (43 Terabytes), a strategy was developed at the outset for efficiently using the simulation data, while maintaining the maximum mesoscale resolution of the data. It was decided to (1) restrict the temporal scope to 36 hours bracketing landfall time of the full 96 hours of simulation, (2) restrict the geographical domain to a 1000x1000 grid centered on the landfall location of the full 5320x5000 domain, (3) limit the number of layers to the lowest 50 of 150 layers and (4) dissect only those variables from the output files that were of main interest to the analysis. The 73 WRF archive files of 224 GB each were transferred from NCSA to NCAR via Globus and the subsets of data were extracted from the Network Common Data Form (NetCDF) archive files at NCAR using NetCDF Operators (NCO).

Visualization of both observation and simulation data was done using the NCAR Visualization and Analysis Platform for Ocean, Atmosphere, and Solar Researchers (VAPOR) (Clyne et al. 2007), both its remote access and local workstation versions, as well as using custom-developed Python and matplotlib code. FFmpeg was used for video creation and SeedMe.org (Chourasia et al. 2016) was used for sharing visualized results.

S-2. Observed wind speed adjustments

As mentioned in section 2b, mesonet and NDBC anemometer heights that are not 10 meters are adjusted to 10 meters by fitting a logarithmic wind profile to wind speed averages for stations having anemometers at the two most common heights, 10 and 3 meters, as described below. Although this attempts to account for anemometer height variation among sites, it does not account for surface roughness variation, which is a much greater challenge.

First, the time window for which most stations have valid wind speed observations is discerned, which yields a 24-hour window of 1800 UTC 28 October through 1800 UTC 29 October. The 14 stations that have missing observations in this window are discarded and mean wind speed is calculated for each station during this 24-hour window.

For the two heights (3 and 10 meters) for which there are many stations, the mean speed is calculated to average the impact of roughness length (z_0) variability among stations. There are 31 stations with 10 meter heights and 60 stations with 3 meter heights. The logarithmic wind profile (Stull 1988) is fit to the two "height means" by varying z_0 and friction velocity (u_*) using the wind speed profile algorithm

$$U = u_*/k \ \ln(z/z_0) \tag{1}$$

where U is wind speed, z is its measurement height and k is the von Karman constant. The fit yields realistic values of z_0 (0.5 m) and u_* (2.1 m s^{-1}) and yields the wind speed adjustment algorithm

$$U_{10} = U_Z \ln(10/z_0) \, / \, \ln(z/z_0) = 3U_Z \, / \, \ln(z/0.5) \tag{2}$$

In the above, U_Z is the wind speed measured at height z. It might be argued that the z_0 value of 0.5 meters used in Eq. (2) might be significantly lower than 0.5 meters over open water. However, the ocean is very rough during the period of this analysis and a z_0 value of 0.5 meters for its surface roughness may not be unreasonable (Bowyer and MacAffee 2005, Evans et al. 2017, Gao et al. 2009, Veiga and Queiroz 2015).

S-3. WRF wind profile validation

An important facet of this investigation is using the WRF mesoscale simulation output to aid interpreting the sparser observation data. Thus, to build confidence in the suitability and reasonableness of the simulation data, profiles of simulation variables were compared with profiles of observations from the 3 rawinsonde sites and wind profiles from the WSR-88D site. During 12 hours before landfall, data were available for 4 variables at OKX and WAL at 3 observation times and at IAD at 5 observation times. For the WSR-88D site at DIX, wind observations were used at the 5 observation times comparable to those at IAD, although wind observations are actually available at about 6-minute intervals at DIX.

Simulation and observation profiles were compared to an altitude of 3.5 km for all times and sites as described above. An example comparison at DIX is shown in Fig. S-1. Comparisons were examined visually, since quantitative statistical comparisons of profile data are beyond the scope of this work. For the most part, agreement is reasonable. The only exceptions are that (1) WRF is too early (by about 6 hours) and too high (by about 700 meters) with the easterly low level jet (LLJ) intensification compared to the wind profiles at OKX and DIX and (2) WRF over-predicts the intensification of the westerly LLJ at WAL before landfall time. Both observations and WRF generally show the elevation of LLJ maximum wind speeds in the range of 1 to 2 km, which is somewhat higher than the 0.5 to 1.5 km elevation range obtained from GPS dropwinsonde profiles of other storms (Franklin et al. 2003, Kepert 2006), although the dropwinsonde observations were of storms over the ocean. Interestingly, the elevation range of maximum speeds reported herein is comparable to that of biological scatterer (bird and insect) signatures observed by the DIX radar during Sandy (Van Den Broeke 2013).

S-4. PBL stability

The cool intrusion described in section 3d is exhibited in wind profile observations which suggest that the leading edge of the southern cooler, drier LLJ that encircled the storm center advanced faster aloft over northern New Jersey, destabilizing the boundary layer there. It is hypothesized that this promoted downward momentum transport of easterly LLJ winds that contributed to higher winds over northern portions of the landfall region near and after landfall time. Tongue (2014) noted boundary layer destabilization observed at OKX and its possible role in contributing to higher winds during post-tropical cyclone Sandy and Hewson (2015) discusses similar mechanisms for extratropical cyclones.

To examine PBL stability, the gradient Richardson number (Ri) is used here as the metric. Vertical gradients are calculated between the surface and approximately 1.5 km MSL. The rawinsonde surface elevation is nominally at 0 AGL and the WRF surface is at 2 and 10 meters AGL for potential temperature and wind speed, respectively. Mean potential temperature is calculated among 4 elevations: the surface, 0.3, 0.6 and 1.5 km MSL.

Results are shown in Table S-1 for the 3 rawinsonde sites nearest to landfall and additionally for DIX from the WRF simulation. The lowest Ri values among all sites were at OKX for both observations and the WRF simulation. The observed value of Ri drops to its lowest value of 0.15 at 0000 UTC, which is below the 0.25 threshold for dynamical instability. However, a pre-landfall destabilization below 3 km analogous to that observed at OKX is not exhibited by the WRF simulation. In fact, the observed Ri is always lower than that of the simulation, with the lowest simulation value being 0.52 at 1800 UTC. These comparisons suggest that the WRF simulation may have under-represented vertical eddy flux of momentum and, thus, downward momentum transport from LLJs, which may have accounted for at least some of WRF's under-prediction of wind speed near and around the New York City metropolitan region.

S-5. WRF PBL modeling scheme

As mentioned in section 5b, surface winds predicted by WRF exhibit a significant dependence on location. To aid in interpreting this dependence, a description of the WRF model entities that quantify surface winds is presented here. WRF's three relevant model entities that most directly quantify surface wind speed are the PBL, the surface layer (Businger et al. 1971, Jimenez et al. 2012) and the land surface. The specific modeling schemes used in this work are the YSU PBL scheme (Hong et al. 2006), the MM5 similarity theory surface layer scheme (Zhang and Anthes 1982) and the Noah land surface scheme (Tewari et al. 2004).

The PBL scheme encompasses a number of the lowest model layers. The specific number of layers comprising the PBL depends on the PBL depth, which is determined by the thermal vertical profile of the lower model layers. The vertical momentum flux through the PBL is

parameterized by specifying a vertical profile of the turbulent eddy diffusion coefficient for momentum, K_m, spanning the vertical extent of the PBL. The land surface scheme parameterizes the flux of horizontal momentum to the surface as a friction velocity variable, u_*, which is determined from z_0 and wind speed in the lowest model level. Finally, the surface layer, which lies between the lowest model layer and the land surface, provides the exchange coefficient for momentum, C_d, which is used in the land surface scheme. For stability regimes other than free convection, C_d depends only on z, z_0 and $\mathrm{Ri_b}$, the bulk Richardson number.

WRF's 10 meter wind speed is calculated from the wind speed of the lowest model layer (Jimenez et al. 2012) as

$$u_{10} = u_z \left[\ln(10/z_0) - \psi_m(10/L) \right] / \left[\ln(z/z_0) - \psi_m(z/L) \right] \tag{3}$$

where u_z is the wind speed of the lowest model layer, whose middle is at elevation z, ψ_m is the integrated similarity function for momentum and L is the Obukhov length (Obukhov 1946). The function $\psi_m(z/L)$ is assigned a different form that depends on the value of $\mathrm{Ri_b}$. In this work, $\mathrm{Ri_b}$ ranges between 0.001 and 0.01 for the lowest 300 meters at all 3 rawinsonde sites for most times during 1200 to 0000 UTC and is within the same range for the lowest WRF model layer (the middle of which is at 30 meters) for the same sites and times. If $\mathrm{Ri_b}$ is assumed to be 0.01, for example, then the above equation for 10 meter wind speed becomes

$$u_{10} = u_{30} \left[\ln(10/z_0) + 4.8 \, \mathrm{Ri_b} \ln(10/z_0) \right] / \left[\ln(30/z_0) + 4.8 \, \mathrm{Ri_b} \ln(30/z_0) \right] \tag{4}$$

which depends only on u_{30} (wind speed in the lowest model layer), $\mathrm{Ri_b}$ and z_0.

S-6. Comparison with inundation forecasts

The under (over) prediction of inundation at the New York City metropolitan region (Atlantic City and Cape May) by forecasting models (Forbes et al. 2014) is consistent with the WRF predictions of this work. Herein it is shown that there is an under (over) prediction of wind speed by WRF north of (south of and near) the storm track. Furthermore, WRF predicted a much smaller eye throughout the landfall period compared to observations, yielding a broader area of high winds than observed near Atlantic City. Predicted and observed wind speeds of this work indeed are similar to those of other post-tropical cyclone Sandy inundation studies (Drews and Galarneau 2015, Magnussen et al. 2013). For example, wind speed time series at buoys 44065 and 44025 show that observed and 500 meter resolution WRF peak speeds of this work agree well with 5 km WRF simulations of Magnussen et al. (2013), in both timing and magnitude (25 m s^{-1}).

S-7. Plans

As mentioned in <mark>section 1b</mark>, this work is intended as an initial characterization and foray into understanding surface winds during Sandy's landfall on New Jersey from a broad perspective. Subsequent papers are planned to delve more deeply into specific topics. Areas of study will likely include:

- Quantifying LEC signatures through autocorrelation analysis of observed time series and determination of wave length, speed and direction of LEC signatures by analysis of radar imagery.
- Improving quantification of mesonet wind speeds by adjusting observed wind speeds using USGS land-use roughness-length fields, applying station topographic roughness-length corrections analogous to those developed recently for WRF and accommodating forest canopy height as appropriate for the site.
- Verifying WRF with observations in more detail such as among hill, plains and valley station locations and across boundaries of USGS land-use roughness length.
- Quantifying the reach inland from the coastline of onshore higher winds, similar to the current preliminary studies for Lewis, DE and Raritan Bay.
- Characterizing the warm wind speed dart in its circulation structure, evolution and potential role of influencing wind fields over land.

TABLE S-1. PBL stability comparisons, where the entries are values of the gradient Richardson number (Ri) calculated between the surface and approximately 1.5 km MSL. The 3 times are for 12 and 6 hours before landfall on 29 October 2012 and at nominal landfall time on 30 October 2012. Bold entry denotes minimum value of gradient Richardson number.

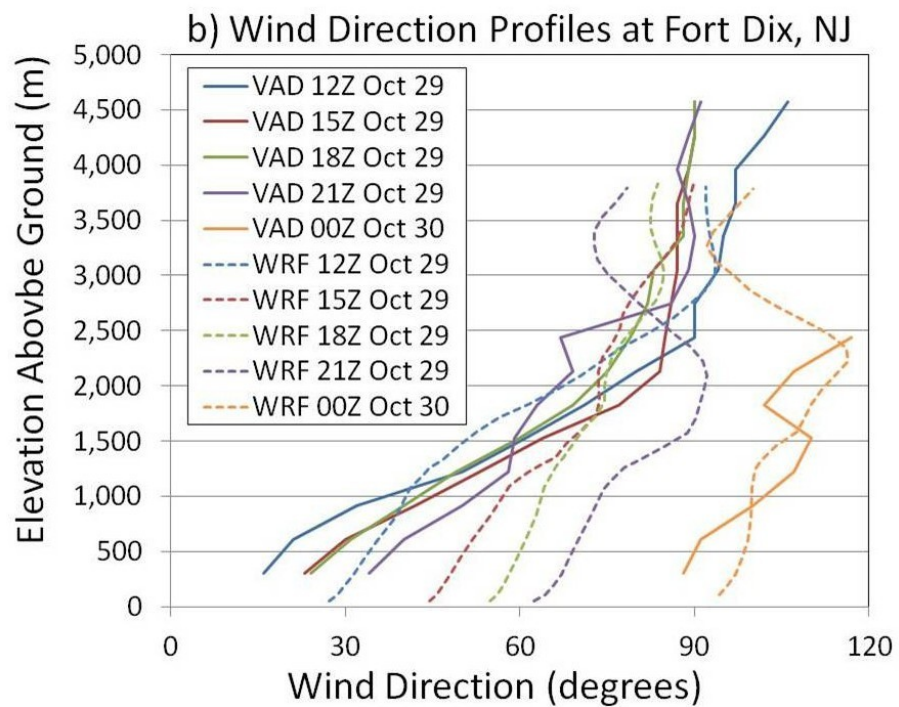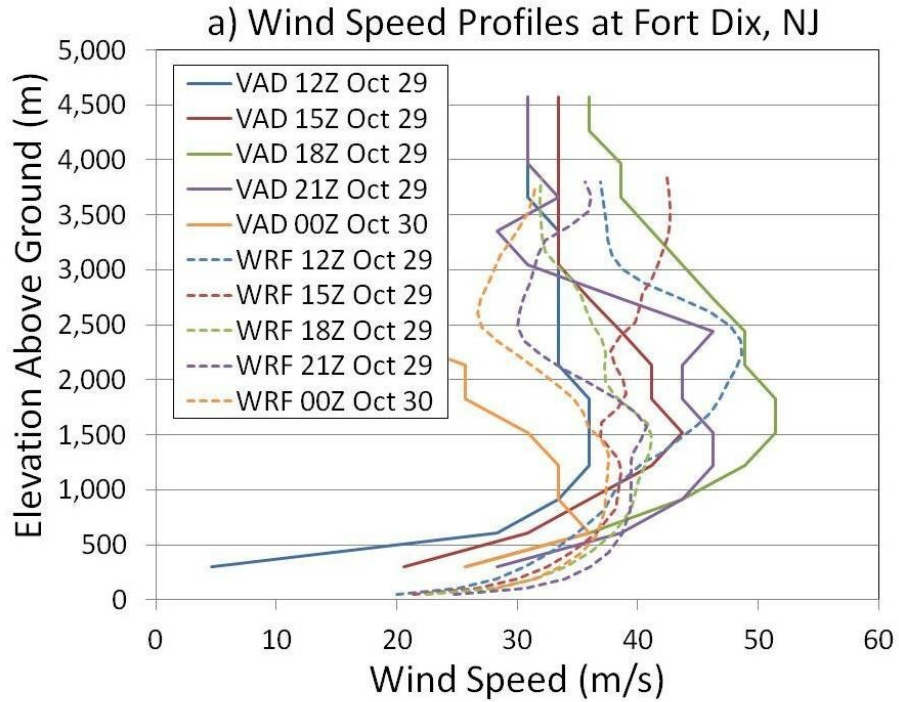| Sounding	Observations			Simulation		
Time (UTC)	1200	1800	0000	1200	1800	0000
OKX	0.44	0.30	**0.15**	0.68	0.52	0.64
DIX	–	–	–	0.66	0.68	5.85
WAL	7.84	1.18	14.11	1.16	1.15	0.75
IAD	1.88	0.66	0.45	4.61	2.08	1.17

FIG. S-1. Observed and WRF simulation profiles of wind (a) speed and (b) direction at Fort Dix, NJ, where the site is located on Fig. 1 as the orange triangle in central New Jersey. Profiles are shown at 3 hour intervals during 12 hours ending at landfall time. Observations are solid and simulation results are broken lines.

FIG. S-2. Fort Dix, NJ (DIX) WSR-88D observed radar reflectivity at 305 meter elevation for 24 hours beginning at 1200 UTC 29 October 2012.

FIG. S-3. Animation of Fig. 6: Cool air encirclement of post-tropical cyclone Sandy core illustrated by simulated 294 K potential temperature 3-D iso-surface below 4 km elevation for 36 hours beginning at 0000 UTC 29 October 2012. Elevation of iso-surface is denoted by colors.

FIG. S-4. Top view of simulated surface temperature at 2 meter elevation (colors and contours) and vertical cross sections of potential temperature (colors). Animation range is 1800 UTC 28 October 2012 to 1200 UTC 30 October 2012 with 30 minute frame interval. Horizontal domain is 30.7797 to 41.7093 degrees North latitude and -77.0663 to -67.1202 degrees West longitude and cross section height is 10 km. Surface temperature color range is 279.5 (violet) to 293.7 (red) K and contour range is 285 (black) to 295 (white) K with an interval of 2 K. Potential temperature vertical cross section color range is 280 (violet) to 340 (red) K.

FIG. S-5. Animation of Fig. 7: Simulated 34 m s^{-1} wind speed 3-D iso-surface below 7 km elevation from 1500 UTC 29 October 2012 to 1200 UTC 30 October 2012 at 3 hour intervals. Elevation of iso-surface is denoted by colors.

FIG. S-6. Top view of simulated surface wind speed at 10 meter elevation (colors), surface temperature at 2 meter elevation (contours) and horizontal streamlines at 10 meter elevation with vertical cross sections of wind speed (colors). Animation range is 1800 UTC 28 October 2012 to 1200 UTC 30 October 2012 with 30 minute frame intervals. Horizontal domain is 30.7811 to 41.7077 degrees North latitude and -77.0661 to -67.1206 degrees West longitude and cross section height is 10 km. Surface wind speed color range is 0 (violet) to 30 (red) m s^{-1} and surface temperature contour range is 284 (black) to 298 (white) K with an interval of 2 K. Streamline surface temperature color range is 290.6 (violet) to 301.5 (red) K. Wind speed vertical cross section color range is 7 (violet) to 44 (red) m s^{-1}.

FIG. S-7. Animation of Fig. 8a: Top view of simulated surface wind speed at 10 meter elevation (colors), surface temperature at 2 meter elevation (contours), and vertical cross sections of wind speed (colors). Animation range is 1800 UTC 28 October 2012 to 1200 UTC 30 October 2012 with 30 minute frame intervals. Horizontal domain is 30.7811 to 41.7077 degrees North latitude and -77.0661 to -67.1206 degrees West longitude and cross section height is 10 km. Surface wind speed color range is 0 (violet) to 30 (red) m s^{-1} and surface temperature contour range is 284 (black) to 298 (white) K with an interval of 2 K. Wind speed vertical cross section color range is 7 (violet) to 44 (red) m s^{-1}.

FIG. S-8. South view of simulated potential temperature (colors) and vertical velocity (contours) at 300 meter elevation for warm wind speed dart. Violet is coolest and red is warmest potential temperature. Black is downward and white is upward vertical velocity. Chesapeake Bay is at middle left edge and Delaware Bay is in upper left corner. At top is vertical cross section of potential temperature field using same color scale as for 300 meter elevation horizontal plane.

FIG. S-9. Animation of Fig. 13a: Fort Dix, NJ (DIX) WSR-88D observed radar radial base velocity at 0.5 degrees elevation angle for 24 hours beginning at 1200 UTC 29 October 2012. Green is velocity toward radar station and red is away from it.

FIG. S-10a. Simulated radar reflectivity for 9 hours beginning at 1800 UTC 29 October 2012, with domain and colors approximately corresponding to those shown in observed radar reflectivity visualization (Fig. S-2).

FIG. S-10b. South view of vertical wind component at several elevations with surface wind speed at 10 meter elevation (semitransparent colors) at 2100 UTC 29 October 2012. Animation elevations for wind speed are 200, 300, 400, 500, 600, 700, 1500, 2500 and 3500 meters. Horizontal domain is 37.4083 to 41.8259 degrees North latitude and -77.4211 to -71.5020 degrees West longitude. Vertical wind component colors are -0.6 to -0.36 (blue) and 0.36 to 0.6 (red) m s^{-1}. Surface wind speed color range is 9 (violet) to 32 (red) m s^{-1}.

FIG. S-11. Animation of Fig. 15a: Simulated surface wind speed at 10 meter elevation (colors) for 36 hours beginning at 0000 UTC 29 October 2012 and observed surface winds indicated by barbs. Frame interval is 30 minutes, each full barb is 10 m s^{-1} and each half barb is 5 m s^{-1}.

FIG. S-12. Simulated wind speed at 202 meter elevation (colors) for 24 hours beginning at 0600 UTC 29 October 2012 and observed surface winds indicated by barbs. Frame interval is 30 minutes, each full barb is 10 m s^{-1} and each half barb is 5 m s^{-1}.